Digital Predistortion of Frequency-Multipliers-Based Wideband Millimeter-Wave Sources

by

Ifrah Jaffri

A thesis
presented to the University of Waterloo
in fulfillment of the
thesis requirement for the degree of
Master of Applied Science
in
Electrical and Computer Engineering

Waterloo, Ontario, Canada, 2020

© Ifrah Jaffri 2020

I hereby declare that I am the sole author of this thesis. This is a true copy of the thesis, including any required final revisions, as accepted by my examiners.

I understand that my thesis may be made electronically available to the public.

Abstract

Radio frequency (RF) technology has seen unprecedented advancements over the past few decades. These advancements have been driven by continuously growing demand for wireless networks. These demands have been partially addressed using radio communication solutions with operating frequencies predominantly in the giga-hertz (GHz) bands. However, the extensive penetration of radio communication into various industry sectors has spurred a shift to the millimeter-wave (mm-wave) bands, where abundant spectrum resources are available. Yet, this shift brings with it several challenges, especially to the design of RF transceivers. Some of these challenges are due to the increased parasitics and reduced performance (efficiency, output power, gain) of most of the semiconductor technologies as the operating frequency increases. Others are associated with the propagation at mm-wave which is characterised with significant losses.

In this work, a frequency multipliers-based high frequency, wideband and high quality signal transmitter (TX) architecture is proposed which outperforms power amplifier (PA)-based TXs. Nevertheless, some linearization techniques, for example digital predistortion (DPD), have to be deployed to mitigate the distortions caused by frequency multipliers in the TX chain. This thesis proposes a novel DPD scheme for mitigating the effects of nonlinear distortion caused by frequency multipliers when driven with wideband vector modulated signals. An effective pruning strategy is applied to limit the number of coefficients and consequently limit the complexity of the DPD scheme while maintaining excellent linearization capacity. Extensive tests are conducted using different mm-wave frequency multipliers for proof of concept validation. These multipliers include two frequency doublers (25 GHz, 28 GHz), a tripler (63 GHz), and a quadrupler (25 GHz), and are driven by vector modulated signals with an instantaneous bandwidth (BW) of up to 400 MHz. With 44 coefficients or less, the proposed DPD allowed for excellent cancellation of the distortions exhibited by the frequency doublers and improved the error vector magnitude (EVM) and adjacent channel power ratio (ACPR) from about 21% and 21 dB to 1.8-0.8% and 47-54 dB for the different test signals. Similarly, in the case of the frequency tripler, the EVM and ACPR improved from 8% and 30 dB to less than 1.7% and 45-51 dB after applying the proposed DPD scheme with 57 coefficients for the different test signals

used. Finally, in the case of the frequency quadrupler, which is composed of a cascade of two frequency doublers, the proposed DPD scheme was able to achieve similar quality of output signal with higher number of coefficients.

Moreover, the considerable free-space path loss at mm-wave frequencies motivates the use of large-scale multiple antenna (LSMA) TX architectures to improve the radiation output power and beam-steering capability. In this work, a frequency-multipliers-based radio frequency (RF) beamforming architecture suitable for the generation/transmission of high-frequency vector-modulated signals is proposed. Additionally, in order to tackle the nonlinearity of the frequency multipliers, the proposed architecture incorporates a single-input-single-output (SISO) DPD function that has been carefully synthesized to guarantee excellent EVM and ACPR for the signals received in the far-field. A 2×2 beamforming array was built using off-the-shelf frequency doublers and printed circuit board based patch antennas, all operating at 28 GHz, to serve as the device-under-test (DUT) in the validation experiments. Over-the-air (OTA) experiments confirmed the ability of the proposed architecture to successfully generate orthogonal frequency division multiplexing (OFDM) signals. For instance, EVMs as low as 0.9% and 2.5% and ACPRs equal to 52 dB and 47 dB, were obtained for modulation BWs equal to 100 MHz and 400 MHz, respectively.

Acknowledgements

Dedication

This thesis is dedicated to my parents Saghir Jaffri, Nayyar Khursheed, my aunt Kanwal Khursheed and the rest of my family members for their non-stop emotional and spiritual support and care.

Table of Contents

List of Tables

List of Figures

Abbreviations

f_{max} maximum oscillation frequency 2, 6, 7

3GPP third generation partnership project 57

5G fifth generation 1

ACPR adjacent channel power ratio iii, iv, x, xi, xiii, xiv, 9, 32–41, 53–58, 60–62, 64, 65

ADC analog-to-digital converter 67

AF array factor 44, 60

BPF band pass filter 31

BPSK binary phase shift keying 6

BW bandwidth iii, xi–xiv, 1, 5, 6, 8–11, 21, 31, 34–36, 39, 41, 53, 56–62, 67

CBBE complex baseband equivalent 3, 13, 14, 18, 22, 50, 51, 66

CW continuous wave 44

DAC digital-to-analog converter 29, 46, 67

DPD digital predistortion iii, iv, vii, viii, x–xiv, 2, 3, 9–11, 18, 22, 23, 28–32, 34–37, 39, 41, 46–49, 51, 53–62, 64–67

QAM quadrature amplitude modulation 1, 6–9, 31, 53, 60, 66

QPSK quadrature phase shift keying 6

RF radio frequency iv, viii, xii, 1–3, 11–13, 31, 45–53, 64, 66

RX receiver xiii, xiv, 10, 42, 52, 53, 56–59, 62

SISO single-input-single-output iv, xii, xiv, 2, 3, 47–50, 56–58, 60, 64–67

TOR transmitter observation receiver 54

TX transmitter iii, iv, viii, x, xi, xiii, xiv, 2, 3, 5–10, 30, 41–43, 45, 46, 48, 52, 54, 55, 57–62, 67

Chapter 1

Introduction

Wireless mobile communication technology has experienced significant growth to respond to the continuous demands for increased data throughput and system capacity. Traditionally, each generation of wireless communication has occupied the sub-6 GHz RF bands. However, the recently envisaged ultra-reliable low latency communication and enhanced mobile broadband services for fifth generation (5G) of wireless communication call for greater data-bandwidth that can not be met using the crowded sub-6 GHz bands. This has motivated the shift to the untapped mm-wave and sub-terahertz (THz) frequency ranges (30-300 GHz), which provide vast unallocated frequency bands that can support ultra-fast wireless communication. This shift is one of the key technologies of 5G and enables the transmission of communication signals with modulation BW up to hundreds of megahertz (MHz). This facilitates the wideband communication system to achieve high data rate (up to multi-gigabit per second (Gb/s)), low latency and reliable communication.

Moreover, besides increasing the modulation BW of the signal, the data rate of wireless communication can be increased by using complex modulation schemes. Therefore, the throughput of the system can be increased by using higher order modulation schemes such as 64-quadrature amplitude modulation (QAM), 256-QAM and multi-carrier scheme based signals such as OFDM. However, such spectrally efficient signals have higher peak-to-average power ratio (PAPR). As a result, the input power has to be backed off in order to achieve good signal quality by avoiding nonlinear distortion. Operating PAs in back

off region would result in lower output power and lower power efficiency. Conversely, to operate the PA in a power efficient region and to diminish the nonlinear distortions, the linearization techniques such as, DPD schemes have been widely used in the literature.

Unfortunately, transmitting high quality and wideband signals at mm-wave and sub-THz frequency bands poses serious challenges. These challenges are to a large extent attributable to i) the increased parasitics and reduced RF performance (efficiency, output power, gain) of most semiconductor technologies as the operating frequency increases [4], and ii) high propagation losses at mm-wave frequencies.

The first problem of low RF performance of semiconductor devices, yielding low power efficiency and low output power at the TXs, is mainly due to transistor maximum oscillation frequency (f_{max}) of the underlying PAs. A PA based TX is limited in its performance as the carrier frequency reaches f_{max} [5,6]. In order to tackle this challenge, this thesis proposes a frequency multiplier based TX architecture. A DPD scheme is also proposed to mitigate the distortions caused by frequency multipliers in the TX chain.

The later challenge of high propagation loss at high frequencies has also interested a significant amount of recent research studies at different design levels. This has included developing sub-micron semiconductor fabrication processes with improved active and passive components, and new circuit topologies with improved RF performance at the device and circuit levels that have reduced parasitic losses and ultimately more output power. At the radio system design level, various LSMA architectures were reported in the literature which direct the transmitted signals to an intended direction and maximize the radiation gain. These architectures usually fall into one of three categories: digital, RF or hybrid beamforming architectures. At mm-wave frequencies, RF beamforming architectures have been the most popular as they offer the lowest complexity and cost compared to their counterparts [7,8]. This thesis proposes a frequency-multipliers-based RF beamforming TX architecture to address the problem of high frequency signal generation with higher gain. A SISO DPD scheme is also proposed to compensate for the non-idealities of the frequency multiplier array.

2

1.1 Thesis Objective

This thesis is proposed to:

- Investigate a DPD scheme capable of mitigating the nonlinear distortions exhibited by frequency-multipliers-based TX, when generating high frequency and wideband vector modulated signals.

- Research a frequency-multipliers-based beamforming TX architecture to increase the radiated power while maintaining acceptable quality of signal in the far-field.

1.2 Thesis Organization

This thesis is organized into the following chapters. First, Chapter 2 discusses literature review on different high frequency vector modulated signal TX architectures. Afterwards, a theoretical and experimental study on the DPD scheme for frequency multipliers is presented. Extensive lab test results, with different frequency multipliers with different multiplication factor at different operating frequencies from different manufacturers and technologies, are also provided to support the proposed novel DPD scheme and prove the generality of the proposed idea. Chapter 3 then proposes a frequency multiplier-based RF beamforming architecture for vector modulated signals. A SISO DPD scheme to linearize the frequency multiplier array is also proposed and verified through various experiments. Lastly, a summary of the thesis and the potential future works are concluded in Chapter 4.

Note on notation: In this paper, the following notation will be used. A continuous-time RF signal is represented as $x_{RF}(t)$. The complex baseband equivalent (CBBE) of $x_{RF}(t)$ is given as $\tilde{x}(t)$. The discrete-time passband version of $x_{RF}(t)$ is given as $x_{RF}[n]$ while its discrete-time CBBE version is denoted as $\tilde{x}[n]$. Vectors are denoted in bold, i.e., $\mathbf{x}$ and additionally, $\mathbf{x}_{RF}[n]$ and $\tilde{\mathbf{x}}[n]$ represent vectors containing $M + 1$ samples, such that, $\mathbf{x}_{RF}[n] = (x_{RF}[n], x_{RF}[n-1], \ldots, x_{RF}[n-M])$ and $\tilde{\mathbf{x}}[n] = (\tilde{x}[n], \tilde{x}[n-1], \ldots, \tilde{x}[n-M])$. Notation such as $\sqrt[P]{\tilde{\mathbf{x}}[n]}$ indicates element-wise rooting, i.e., $\sqrt[P]{\tilde{\mathbf{x}}[n]} = (\sqrt[P]{\tilde{x}[n]}, \sqrt[P]{\tilde{x}[n-1]}, \ldots, \sqrt[P]{\tilde{x}[n-M]})$. The real and imaginary parts of a complex variable

x are denoted by $\Re\{x\}$ and $\Im\{x\}$, respectively. The complex conjugate of x is denoted by x^*. Likewise $\tilde{x}^{*\frac{1}{2}}$ denotes $(\tilde{x}^*)^{\frac{1}{2}}$ and for a real number c, $\tilde{x}^{*c}$ denotes $(\tilde{x}^*)^c$. The symbol $:=$ indicates equality by definition and for integers a and b, $a|b$ indicates that a divides b, i.e., $3|6$.

Chapter 2

Theoretical and Experimental Study on Digital Predistortion for Frequency Multipliers

2.1   Literature Review

Fig. 2.1 shows three TX architectures which have been considered in the literature at high frequency ranges. These include: i) a TX architecture with last stage power amplifier (PA), ii) a nonlinear mixer based TX architecture, and iii) a TX architecture with last stage frequency multiplier.

The first architecture, depicted in Fig. 2.1a, uses an upconversion mixer followed by a PA as a last stage. However, the limited performance of the PAs at these frequency ranges (low power, low efficiency, nonlinearity), restricts the application of this architecture to generating low-order modulation schemes so that the resulting signals have either constant envelope or low envelope variation [9–18]. The authors in [9] demonstrated TX architecture at 300 GHz, while, in [10], the authors demonstrated a TX centered at 240 GHz, with 40 GHz TX BW and an output power of 6 dBm. Both in [9] and [10], the local oscillator (LO) signal was upconverted using frequency multiplier. However, the results

(a)

$s_{IF/BB}(t)$ $x_{RF}(t)$ $y_{RF}(t)$

Power Amplier

$(.)^D$

LO Source

(b)

$\widetilde{x}_{IF_2}(t)e^{j\omega_{IF_2}t}$
$+ \widetilde{A}_{LO}e^{j\omega_{Lo}t}$

$s_{IF_1}(t)$ $y_{RF}(t)$

Harmonic mixer

$(.)^D$

LO Source

(c)

$s_{IF/BB}(t)$ $x_{RF}(t)$ $(.)^D$ $y_{RF}(t)$

Freq. Multiplier

LO Source
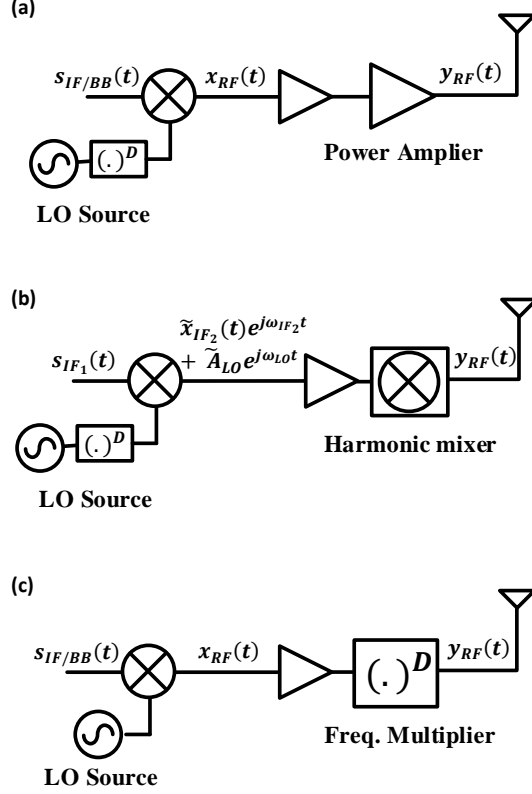
Figure 2.1: (a) TX architecture with last stage PA, (b) nonlinear mixer based TX architecture, where IF$_1$ and IF$_2$ represent first and second intermediate frequencies, respectively, (c) TX architecture with last stage frequency multiplier. Here, $(.)^D$ represents a frequency multiplier of multiplication factor D.

demonstrated were with low order modulation signal such as binary phase shift keying (BPSK) and quadrature phase shift keying (QPSK). The work in [11] demonstrated an ultra-wideband mm-wave 70-105 GHz wireless transceiver (TRX) with modulation BW of 35 GHz. However, the TX output power was quite low. The test signals used were QPSK, 8PSK and 16-QAM. Furthermore, the PA stage imposes a relatively low upper-bound for the operating frequency as the underlying transistor must be operated at a frequency which is significantly lower than its f_{max} frequency.

Alternatively, the second TX architecture (shown in Fig. 2.1b), starts with a modu-

lated signal (centered around an IF_1) that feeds an upconversion mixer. The output of the mixer is further upconverted using a harmonic mixer to generate high frequency modulated signals. This architecture allows the frequency upper-bound to approach f_{max}. This architecture has two intermediate frequencies (IFs). The mixer up-converts the digitally modulated signal at first IF (IF_1) to second IF (IF_2) with high linearity. The harmonic mixer receives a two-tone-like signal composed of modulated IF_2 and a pure LO signal. The harmonic mixer operates in a way that when the two-tone-like input IF_2 signal, $s(t)_{IF_2}$ and LO signal, $s(t)_{LO}$ is cubed (in case of cubic mixer), first to third order signals (in IF_2) are generated, given in (2.1). Afterwards, the second sub-harmonic mixing term, $3.\tilde{s}_{IF_2}[n]\tilde{s}_{LO}^2[n]e^{j(\omega_{IF_2}+2\omega_{LO})t}$ can be made dominant by carefully tuning the power levels of $s(t)_{IF_2}$ and $s(t)_{LO}$.

$$(s(t)_{IF_2} + s(t)_{LO})^3 =$$
$$s^3(t)_{IF_2} + 3.s^2(t)_{IF_2}.s(t)_{LO} + 3.s(t)_{IF_2}.s^2(t)_{LO} + s^3(t)_{LO}$$

The baseband equivalent form is given as,

$$= \Re\left\{\tilde{s}_{IF_2}^3[n]e^{j3\omega_{IF_2}t}\right\} + 3.\Re\left\{\tilde{s}_{IF_2}^2[n]e^{j2\omega_{IF_2}t}\right\}.\Re\left\{\tilde{s}_{LO}[n]e^{j\omega_{LO}t}\right\}$$
$$+ 3.\Re\left\{\tilde{s}_{IF_2}[n]e^{j\omega_{IF_2}t}\right\}.\Re\left\{\tilde{s}_{LO}^2[n]e^{j2\omega_{LO}t}\right\} + \Re\left\{\tilde{s}_{LO}^3[n]e^{j3\omega_{LO}t}\right\}$$

Ignoring the conjugate terms and third order harmonics give,

$$= 3.\tilde{s}_{IF_2}^2[n]e^{j2\omega_{IF_2}t}.\tilde{s}_{LO}[n]e^{j\omega_{LO}t}$$
$$+ 3.\tilde{s}_{IF_2}[n]e^{j\omega_{IF_2}t}.\tilde{s}_{LO}^2[n]e^{j2\omega_{LO}t}$$
$$= 3.\tilde{s}_{IF_2}^2[n]\tilde{s}_{LO}[n]e^{j(2.\omega_{IF_2}+\omega_{LO})t} + 3.\tilde{s}_{IF_2}[n]\tilde{s}_{LO}^2[n]e^{j(\omega_{IF_2}+2\omega_{LO})t}$$

$$(2.1)$$

Harmonic mixer based TX architecture has been adopted in [19,20] to generate digitally modulated signals with carrier frequencies of up to 300 GHz. The authors in [19] presented a 300 GHz TX, capable of 32-QAM signal transmission. Here, the operating frequency was

closed to transistor $f_{\max}$ so they chose a PA-less TX architecture using cubic mixer.The work in [19] demonstrated that term $3.\tilde{s}_{IF_2}[n]\tilde{s}_{LO}^2[n]e^{j(\omega_{IF_2}+2\omega_{LO})t}$ in (2.1) preserves the linearity of IF_2 while upconversion. This is one of the main advantage of using harmonic or sub-harmonic mixer in TX architecture that it preserves the linearity of the original signal. Moreover, unlike frequency multipliers in TX chain, no signal bandwidth expansion occurs here. Also the work in [19] shows that the cubic mixer is as compact size as the triplers. But the reported output power is very poor. Similarly, the authors in [20] used square mixer in TX chain and used higher order modulation signals (32-QAM and 128-QAM) with an operating frequency of 300 GHz. Unlike [19], they used frequency doublers so higher output power was achieved because the metal oxide semiconductor field effect transistor (MOSFET) quadratic nonlinearity is stronger than cubic counterpart. The peak output power of their TX is -5.5 dBm. However, the mixing results as unwanted spurious (e.g. doubled or tripled LO, unwanted mixing products and image that cause interference). Some of these spurious are near to the frequency band of interest hence the harmonic mixer based TX architecture requires a higher order filter after upconversion or/and additional signal processing and hardware requirement. To mitigate these limitations, the authors of [21–25] devised a new architecture where the harmonic mixer is replaced by a frequency multiplier (Fig. 2.1c). [21] and [24] showed results with phase modulated signals, where [24] had 240 GHz center frequency, 80 GHz BW and 0 dBm output power. The authors in [22] developed and discussed 3D imaging using sub-mm-wave frequency modulated continuous wave (FMCW) radar system operating near 600GHz. Similarly, the authors in [23] used frequency multiplier with FMCW signal in automotive RADAR. The frequency operating range was 76-81 GHz. Also, the work in [25] used frequency multiplier to generate 77 GHz signal with output power of 8.9 dBm. While this third architecture allows for reaching higher frequencies, it has been mainly applied to generating modulated signals with constant envelope and limited spectral efficiency.

The adoption of the above mentioned three architectures when generating high modulation order and multi-carrier (OFDM) signals was hindered by the inherent nonlinear distortion exhibited by the last stages. This is particularly the case of the third architecture where the frequency multiplier generally exhibit significant distortions. To address this issue, the authors in [26,27] augmented the third TX architecture with the outphasing

8

concept so that signal generation can be performed using nonlinear frequency multipliers based architectures. Work in [26] demonstrated frequency multiplier based 216 GHz TX architecture with 16-QAM modulated test signal. The authors took inspiration from linear amplification using nonlinear components (LINC) architecture [28]. Like outphasing technique, the amplitude varying signal was decomposed into two phase modulated signal and passes through two parallel chain of frequency multiplier followed by a PA. Since the two signals are constant envelope, none of the distortion can be seen at the output of two chains. The two output signals are then combined to get high power and high frequency amplitude modulated signal. This outphasing technique was further explored by [27] at mm-wave frequency of 25 GHz. The author in [27] used OFDM signal and applied to wide band signals (modulation BW of 80 MHz and 160 MHz). Also, noticeable here that wider modulation bandwidth showed a compromised ACPR and normalized mean square error (NMSE). Hence, generation of ultra wideband signal using this architecture may not be wise because the output signal quality became sensitive to non-idealities exhibited by system components. Additionally, a drawback of this technique is that due to signal separation in outphasing technique, bandwidth expansion occurs. Also, in order to avoid phase and amplitude imbalance between the two paths, additional calibration steps are required in this architecture. Therefore, while the resulting outphasing-based TX allowed for successful generation of OFDM signals, the BW expansion brought about by outphasing poses serious challenges that complicates the design of the building blocks and increases the sensitivities to the imbalance between the different branches. When frequency multipliers are driven by spectrally efficient signals exhibiting high PAPR characteristics, significant nonlinear distortions are produced. To mitigate these nonlinear distortions, the linearization techniques such as, DPD schemes used for linearizing PAs, motivate it's investigation for linearizing the frequency multipliers as well.

In [29–35], memoryless DPD schemes were used to mitigate the distortion exhibited by the frequency multiplier in the third architecture. Using simple look up table (LUT) and polynomial based DPD models, good linearization capacity was demonstrated for low frequency and narrowband signals. The authors in [29] investigated and implemented LUT polynomial based DPD model on frequency multiplier. The results showed good linearization performance but that linearization was done when operating with low carrier

9

frequency i.e., 2.46 GHz and narrowband signals i.e., 20 MHz. Also, this DPD model only corrects the memoryless nonlinearity of the device. Additionally, the phase multiplication process should be nonlinear, but this model treats it as linear. The same authors afterwards expanded the idea presented in [29] with dual band TX [30] but unfortunately with narrowband low frequency signals. The authors in [31, 32] also presented dual band glsTX using LUT based memoryless DPD technique. The work in [33] demonstrated high frequency 75-110 GHz W-band frequency multiplier linearization based on memoryless DPD model. Furthermore, although LUT-based DPD is simple to implement, it becomes much complicated and multi-dimension problem when dynamic memory effects of the device is considered. Hence, if higher signal bandwidth where memory effect is not negligible and higher order modulation are encountered, it will be less effective.

Furthermore, the authors in [36] proposed a DPD scheme that employs a cascade of two memory polynomial functions in order to tackle dynamic nonlinearity exhibited by the frequency quadruplers when driven by signals with wider BWs operating at output frequency of 3.86 GHz. Although the results shown were good, the model was tested on low frequency and relatively narrowband signals. In [37], a phase divider based predistorter (PD) was proposed to pre-process an 8x phase shift keying (PSK) modulated signal in order to alleviate the distortions exhibited by a sixtupler. This solution required additional signal processing at the RX side to mitigate the residual distortions. Recently, [1] and [38] have demonstrated promising linearization capacity using a DPD scheme with memory basis. It is to note that both schemes in [1, 36] and the choice of the underlying basis heavily relied on the direct application of the knowledge accumulated in the context of PA linearization. Furthermore, the DPD synthesis exploited the similarity between the PA post- and pre-distortion functions and applied similar pruning strategies. Unfortunately, this resulted in linearization capacity that reduces with the increase of the frequency multiplication factor and the broadening of the modulation BW, particularly for high input power levels.

In this work, the distortions exhibited by the frequency multiplier are modeled as an additive error using a passband Volterra series expression. Furthermore, careful application of passband to baseband signal conversion and mathematical approximations allowed the derivation of a single-function DPD scheme that incorporates new nonlinear basis that were omitted in previous works. A frequency multiplication factor dependent pruning strategy

10
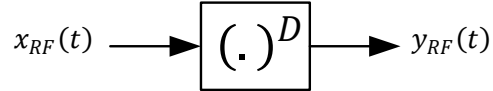
Figure 2.2: Non-ideal Passband Frequency multiplier system.

is also applied to reduce the required number of coefficients and improve the numerical stability. Proof-of-concept experiments have demonstrated the excellent capacity of the new DPD scheme to linearize the behaviors of two frequency doublers, a tripler and a quadrupler, all operating at mm-wave frequencies and driven by modulated signals with instantaneous BW of up to 400 MHz.

2.2 Complex Baseband Equivalent Model Formulation and Proposed DPD Scheme Derivation

2.2.1 Passband Forward Model for Frequency Multiplier

In this sub-section, a passband frequency multiplier expression is introduced to model the dynamic nonlinear behaviour of frequency multiplier with a multiplication factor of D. Fig. 2.2 shows a functional block diagram of a frequency multiplier, where $x_{RF}(t)$ and $y_{RF}(t)$ represent the passband input and output signals, respectively. Let $x_{RF}[n] = x_{RF}(n/F_s)$ and $y_{RF}[n] = y_{RF}(n/F_s)$ be the discrete-time passband output signals where F_s is the sampling rate. Specifically, using the discrete-time Volterra series based expression, the output $y_{RF}[n]$ is modeled as a linear combination of all possible products of k (possibly repeated) terms from the set $\{x_{RF}[n], x_{RF}[n-1], \ldots, x_{RF}[n-M]\}$, where k ranges over $D \leq k \leq N$, and N and M designate the maximum nonlinearity order and the memory depth of the forward model. Note that N and M are integers. Letting $\mathcal{A}_k^M$ denote the set of such RF basis functions for a given order k and memory depth M ($\mathcal{A}_k^M$ is formally

defined in (2.5) below), then the RF output of the frequency multiplier is modeled by

$$y_{RF}[n] = \sum_{k=D}^{N} \sum_{i=1}^{|\mathcal{A}_k^M|} \alpha_{k,i} \phi_{k,i}^M(\mathbf{x}_{RF}[n]), \qquad (2.2)$$

where $\alpha_{k,i}$ are the coefficients, and $\phi_{k,i}^M(\mathbf{x}_{RF}[n])$, $i \in \{1, 2, \dots, |\mathcal{A}_k^M|\}$ enumerates the basis functions in $\mathcal{A}_k^M$. These basis functions are given by

$$\phi_{\mathbf{c}}(\mathbf{x}_{RF}[n]) := \prod_{i=0}^{M} (x_{RF}[n-i])^{c_i}, \qquad (2.3)$$

where the vector $\mathbf{c}$ is constrained to belong to the set $\mathcal{C}_k^M$ given by

$$\mathcal{C}_k^M := \left\{ \mathbf{c} \in \{0, 1, 2, \dots k\}^{M+1} \;\middle|\; \sum_{i=0}^{M} c_i = k \right\}. \qquad (2.4)$$

Then, the set of RF basis functions $\mathcal{A}_k^M$ of order k and memory depth M is given by

$$\mathcal{A}_k^M := \left\{ \phi_{\mathbf{c}}(\mathbf{x}_{RF}[n]) | \mathbf{c} \in \mathcal{C}_k^M \right\}. \qquad (2.5)$$

In (2.2), orders $k < D$ are not included as these product terms can not contribute to the RF output at the desired frequency.

2.2.2   Augmented D^{th} order Volterra Series Construction

The passband discrete-time Volterra series, given in (2.2), is complex due to the significant number of terms included when $N > D$. Alternatively, one can start with the Dth order Volterra series (i.e., choosing $N = D$ in (2.2)), and augment it with a limited set of additional higher order terms, with the resulting set of basis functions called the augmented order D Volterra series.

Hence, we start by first including the Dth order Volterra series terms $\mathcal{A}_D^M$, defined in (2.5), that are comprised of all D-fold products from the set $\{x_{RF}[n], x_{RF}[n-1], \dots, x_{RF}[n-M]\}$. We then augment these basis functions by increasing the order of only one single delay term in any of these original bases. Specifically, to obtain basis functions of order

$k > D$, for each basis function $\phi \in \mathcal{A}_D^M$, we create new basis functions by multiplying ϕ by $x_{RF}[n-m]^{k-D}$ for all possible delays m between 0 and M, and each such product is a new basis function. This also has the effect of limiting the number of unique delays in the basis functions to at most $D+1$.

Subsequently, the RF basis functions are given by,

$$\psi_{\mathbf{c},k}^{D,m}(\mathbf{x}_{RF}[n]) := (x_{RF}[n-m])^{k-D} \prod_{i=0}^{M} (x_{RF}[n-i])^{c_i}, \tag{2.6}$$

where m with $0 \le m \le M$ is the delay who's order is increased and $\mathbf{c} \in \mathcal{C}_D^M$. Then, the set of all such basis functions of order k is given by,

$$\mathcal{Q}_k^{M,D} = \left\{ \psi_{\mathbf{c},k}^{D,m}(\mathbf{x}_{RF}[n]) \middle| \mathbf{c} \in \mathcal{C}_D^M, m \in [0,1,\ldots,M] \right\}. \tag{2.7}$$

Let $\psi_{k,i}^{M,D}(\mathbf{x}_{RF})$, $i \in \{1,2,\ldots,|\mathcal{Q}_k^{M,D}|\}$ enumerate the elements of $\mathcal{Q}_k^{M,D}$. Then the augmented discrete-time Volterra series of order D can be written as,

$$y_{RF}[n] = \sum_{k=D}^{N} \sum_{i=1}^{|\mathcal{Q}_k^{M,D}|} \gamma_{k,i} \psi_{k,i}^{M,D}(\mathbf{x}_{RF}[n]), \tag{2.8}$$

where $\gamma_{k,i}$ are the Volterra coefficients and N is the highest included nonlinearity order.

Complex Baseband Equivalent Model Derivation of the augmented discrete-time Volterra series of order D

The passband signals $x_{RF}[n]$ and $y_{RF}[n]$ are related to their CBBE signals, $\tilde{x}[n]$ and $\tilde{y}[n]$, as well as their angular frequencies, ω_c and $D\omega_c$, by:

$$x_{RF}[n] = \Re\left\{ \tilde{x}[n]e^{j\omega_c n/F_s} \right\} \tag{2.9}$$

$$= \frac{1}{2}\left(\tilde{x}[n]e^{j\omega_c n/F_s} + \tilde{x}^*[n]e^{-j\omega_c n/F_s} \right).$$

$$y_{RF}[n] = \Re\left\{ \tilde{y}[n]e^{jD\omega_c n/F_s} \right\} \tag{2.10}$$

$$= \frac{1}{2}\left(\tilde{y}[n]e^{jD\omega_c n/F_s} + \tilde{y}^*[n]e^{-jD\omega_c n/F_s} \right).$$

Substituting (2.9) and (2.10) in (2.8) and keeping terms containing $e^{jD\omega_c n/F_s}$ only yields a CBBE model for (2.8). The step-by-step derivation is given in following. The augmented discrete-time passband Volterra series of order D, given in (2.8) can also be written as,

$$y_{RF}[n] = \sum_{k=D}^{N} \sum_{\substack{m' \in [M] \\ \dot{\boldsymbol{m}} \in \mathcal{I}_D}} g(m', \dot{\boldsymbol{m}}, k)(x_{RF}[n - m'])^{k-D} \prod_{i=1}^{D} x_{RF}[n - \dot{m}_i], \qquad (2.11)$$

where $g(m', \dot{\boldsymbol{m}}, k)$ denotes the model kernels, $\mathcal{I}_p$, for any integer p, denotes the set

$$\mathcal{I}_p = \left\{ \mathbf{q} \in \{0, \dots, M\}^p \mid 0 \le q_1 \le \cdots \le q_p \le M \right\},$$
$$[M] = \{0, \dots, M\},$$

m' is an integer and $\dot{\boldsymbol{m}} = [\dot{m}_1, \dot{m}_2, \dots, \dot{m}_D]^T$. Let,

$$y_{RF}[n] = \sum_{k=D}^{N} z_{RF,k}[n], \qquad (2.12)$$

where

$$z_{RF,k}[n] = \sum_{m' \in [M]} (x_{RF}[n - m'])^{k-D} \sum_{\dot{\boldsymbol{m}} \in \mathcal{I}_D} g(m', \dot{\boldsymbol{m}}, k) \prod_{i=1}^{D} x_{RF}[n - \dot{m}_i]. \qquad (2.13)$$

Consider $(x_{RF}[n - m'])^{k-D}$ from (2.13) and using (2.9), we get,

$$(x_{RF}[n - m'])^{k-D} = \left(\frac{\tilde{x}[n - m']e^{j\omega_c \frac{n}{F_s}} + \tilde{x}^*[n - m']e^{-j\omega_c \frac{n}{F_s}}}{2} \right)^{k-D},$$
$$= \sum_{l=0}^{k-D} \gamma_{l,k-D} \, \tilde{x}^{*l}[n - m'] \, \tilde{x}^{k-D-l}[n - m'] \, e^{j\omega_c \frac{n}{F_s}(k-D-2l)}, \qquad (2.14)$$

where $\gamma_{l,k-D}$ is an appropriate coefficient. Considering the second term, $\sum_{\dot{\boldsymbol{m}} \in \mathcal{I}_D} g(m', \dot{\boldsymbol{m}}, k) \prod_{i=1}^{D} x_{RF}[n - \dot{m}_i]$, from (2.13) and using (2.9), we get,

$$\sum_{\dot{\boldsymbol{m}} \in \mathcal{I}_D} g(m', \dot{\boldsymbol{m}}, k) \prod_{i=1}^{D} x_{RF}[n - \dot{m}_i]$$
$$= \sum_{k'=0}^{D} e^{j\omega_c \frac{n}{F_s}(D-2k')} \sum_{\substack{\dot{\boldsymbol{m}} \in \mathcal{I}_{k'} \\ \ddot{\boldsymbol{m}} \in \mathcal{I}_{D-k'}}} \mu_k^{m', \dot{\boldsymbol{m}}, \ddot{\boldsymbol{m}}} \prod_{i=1}^{k'} \tilde{x}^*[n - \dot{m}_i] \prod_{j=1}^{D-k'} \tilde{x}[n - \ddot{m}_j], \qquad (2.15)$$

14

where $\ddot{\boldsymbol{m}} = [\ddot{m}_1, \ddot{m}_2, \ldots, \ddot{m}_{k'}]^T$, $\dddot{\boldsymbol{m}} = [\dddot{m}_1, \dddot{m}_2, \ldots, \dddot{m}_{D-k'}]^T$ and $\mu_k^{m', \ddot{\boldsymbol{m}}, \dddot{\boldsymbol{m}}}$ are coefficients that depend on $g(m', \dot{\boldsymbol{m}}, k)$, . Substituting (2.14) and (2.15) in (2.13), we get,

$$
\begin{aligned}
z_{RF,k}[n] &= \left[\sum_{m' \in [M]} \sum_{l=0}^{k-D} \gamma_{l,k-D} \; \tilde{x}^{*l}[n-m'] \; \tilde{x}^{k-D-l}[n-m'] \; e^{j\omega_c \frac{n}{F_s}(k-D-2l)} \right] \\
&\quad \times \left[\sum_{k'=0}^{D} e^{j\omega_c \frac{n}{F_s}(D-2k')} \sum_{\substack{\ddot{\boldsymbol{m}} \in \mathcal{I}_{k'} \\ \dddot{\boldsymbol{m}} \in \mathcal{I}_{D-k'}}} \mu_k^{m', \ddot{\boldsymbol{m}}, \dddot{\boldsymbol{m}}} \prod_{i=1}^{k'} \tilde{x}^*[n-\ddot{m}_i] \prod_{j=1}^{D-k'} \tilde{x}[n-\dddot{m}_j] \right] \\
&= \sum_{m' \in [M]} \sum_{l=0}^{k-D} \sum_{k'=0}^{D} e^{j\omega_c \frac{n}{F_s}(k-2l-2k')} \; \gamma_{l,k-D} \; \tilde{x}^{*l}[n-m'] \; \tilde{x}^{k-D-l}[n-m'] \\
&\quad \times \sum_{\substack{\ddot{\boldsymbol{m}} \in \mathcal{I}_{k'} \\ \dddot{\boldsymbol{m}} \in \mathcal{I}_{D-k'}}} \mu_k^{m', \ddot{\boldsymbol{m}}, \dddot{\boldsymbol{m}}} \prod_{i=1}^{k'} \tilde{x}^*[n-\ddot{m}_i] \prod_{j=1}^{D-k'} \tilde{x}[n-\dddot{m}_j] \\
&= \sum_{l=0}^{k-D} \sum_{k'=0}^{D} \sum_{\substack{m' \in [M] \\ \ddot{\boldsymbol{m}} \in \mathcal{I}_{k'} \\ \dddot{\boldsymbol{m}} \in \mathcal{I}_{D-k'}}} e^{j\omega_c \frac{n}{F_s}(k-2l-2k')} \; \eta_{l,k,D}^{m', \ddot{\boldsymbol{m}}, \dddot{\boldsymbol{m}}} \; \tilde{x}^{*l}[n-m'] \; \tilde{x}^{k-D-l}[n-m'] \\
&\quad \times \prod_{i=1}^{k'} \tilde{x}^*[n-\ddot{m}_i] \prod_{j=1}^{D-k'} \tilde{x}[n-\dddot{m}_j],
\end{aligned}
\tag{2.16}
$$

where $\eta_{l,k,D}^{m', \ddot{\boldsymbol{m}}, \dddot{\boldsymbol{m}}} = \gamma_{l,k-D} \times \mu_k^{m', \ddot{\boldsymbol{m}}, \dddot{\boldsymbol{m}}}$. We are only interested in the terms that involve the factor $e^{jD\omega_c \frac{n}{F_s}}$. Therefore, only the terms with l and k' such that,

$$
\omega_c(k - 2l - 2k') = D\omega_c,
\tag{2.17}
$$

contributes. From (2.17), we get $\frac{k-D}{2} = l + k'$, which gives a condition that $k - D$ must be even. Also, from (2.17), we get

$$
l = \frac{k-D}{2} - k'.
\tag{2.18}
$$

Fig. 2.3 shows l vs k' as $k' = 0$ to D according to (2.18). When $k' = 0, l = \frac{k-D}{2}$ which is always in range of 0 to $k - D$. When $l = 0, k' = \frac{k-D}{2}$ which may or may not be greater

15

than D. Fig. 2.3 shows two cases, case-1 if $\frac{k-D}{2} \leq D$ and case-2 if $\frac{k-D}{2} > D$. In other words, case-1 occurs when $k \leq 3D$ and case-2 occurs when $k > 3D$.

The minimum value of l for case-1 is 0 while for case-2 is l_{min} where l_{min} can be found by substituting $k' = D$ in (2.18). Hence, $l_{min} = \frac{k-3D}{2}$.

Therefore, for case-1, (2.16) with $k' = \frac{k-D}{2} - l$ becomes (2.19) where $z_{RF,k}^D[n]$ denotes the terms of $z_{RF,k}[n]$ that have $e^{jD\omega_c \frac{n}{F_s}}$ as a factor. Therefore (2.19) is given as,

$$
\begin{aligned}
z_{RF,k}^D[n] &= \sum_{l=0}^{\frac{k-D}{2}} \sum_{\substack{m' \in [M] \\ \ddot{\boldsymbol{m}} \in \mathcal{I}_{k'} \\ \dddot{\boldsymbol{m}} \in \mathcal{I}_{D-k'}}} e^{jD\omega_c \frac{n}{F_s}} \ \eta_{l,k,D}^{m',\ddot{\boldsymbol{m}},\dddot{\boldsymbol{m}}} \tilde{x}^{*l}[n-m']\tilde{x}^{k-D-l}[n-m'] \\
&\qquad\qquad \times \prod_{i=1}^{\frac{k-D}{2}-l} \tilde{x}^*[n-\ddot{m}_i] \prod_{j=1}^{D-\frac{k-D}{2}+l} \tilde{x}[n-\dddot{m}_j] \\
&= \sum_{l=0}^{\frac{k-D}{2}} \sum_{\substack{m' \in [M] \\ \ddot{\boldsymbol{m}} \in \mathcal{I}_{k'} \\ \dddot{\boldsymbol{m}} \in \mathcal{I}_{D-k'}}} e^{jD\omega_c \frac{n}{F_s}} \ \eta_{l,k,D}^{m',\ddot{\boldsymbol{m}},\dddot{\boldsymbol{m}}} |\tilde{x}[n-m']|^{2l}\tilde{x}^{k-D-2l}[n-m'] \\
&\qquad\qquad \times \prod_{i=1}^{\frac{k-D}{2}-l} \tilde{x}^*[n-\ddot{m}_i] \prod_{j=1}^{D-\frac{k-D}{2}+l} \tilde{x}[n-\dddot{m}_j] \\
&= \sum_{l=0}^{\frac{k-D}{2}} \sum_{\substack{m' \in [M] \\ \ddot{\boldsymbol{m}} \in \mathcal{I}_{k'} \\ \dddot{\boldsymbol{m}} \in \mathcal{I}_{D-k'}}} e^{jD\omega_c \frac{n}{F_s}} \ \eta_{l,k,D}^{m',\ddot{\boldsymbol{m}},\dddot{\boldsymbol{m}}} \ \zeta_{l,k,D}^{m',\ddot{\boldsymbol{m}},\dddot{\boldsymbol{m}}}(\tilde{\mathbf{x}}[n]),
\end{aligned}
\tag{2.19}
$$

where we defined

$$
\zeta_{l,k,D}^{m',\ddot{\boldsymbol{m}},\dddot{\boldsymbol{m}}}(\tilde{\mathbf{x}}[n]) = |\tilde{x}[n-m']|^{2l} \ \tilde{x}^{k-D-2l}[n-m'] \prod_{i=1}^{\frac{k-D}{2}-l} \tilde{x}^*[n-\ddot{m}_i] \prod_{j=1}^{D-\frac{k-D}{2}+l} \tilde{x}[n-\dddot{m}_j],
\tag{2.20}
$$

Similarly, for case-2, (2.16) with $k' = \frac{k-D}{2} - l$ becomes,

16
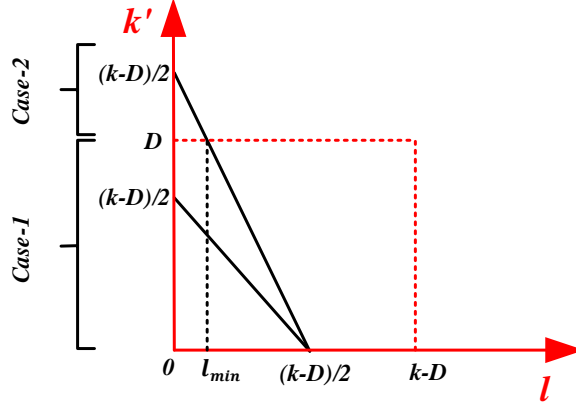
Figure 2.3: Graph of k' vs l in (2.18)

$$z_{RF,k}^{D}[n] = \sum_{l=\frac{k-3D}{2}}^{\frac{k-D}{2}} \sum_{\substack{m'\in[M] \\ \ddot{m}\in\mathcal{I}_{k'} \\ \dddot{m}\in\mathcal{I}_{D-k'}}} e^{jD\omega_c\frac{n}{F_s}}\, \eta_{l,k,D}^{m',\ddot{m},\dddot{m}}\, \zeta_{l,k,D}^{m',\ddot{m},\dddot{m}}(\tilde{\mathbf{x}}[n]). \tag{2.21}$$

Consequently, the combined two cases for maximum nonlinearity order of N, can be expressed by substituting (2.19) and (2.21) in (2.12). Note below that $y_{RF,k}^{D}[n]$ denotes the terms of $y_{RF,k}[n]$ that have $e^{jD\omega_c\frac{n}{F_s}}$ as a factor. The final result is given as,

$$y_{RF}^{D}[n] = \sum_{k\in\mathcal{L}}\sum_{l=0}^{\frac{k-D}{2}} \sum_{\substack{m'\in[M] \\ \ddot{m}\in\mathcal{I}_{k'} \\ \dddot{m}\in\mathcal{I}_{D-k'}}} e^{jD\omega_c\frac{n}{F_s}}\, \eta_{l,k,D}^{m',\ddot{m},\dddot{m}}\, \zeta_{l,k,D}^{m',\ddot{m},\dddot{m}}(\tilde{\mathbf{x}}[n])$$

$$+ \sum_{k\in\mathcal{F}}\sum_{l=\frac{k-3D}{2}}^{\frac{k-D}{2}} \sum_{\substack{m'\in[M] \\ \ddot{m}\in\mathcal{I}_{k'} \\ \dddot{m}\in\mathcal{I}_{D-k'}}} e^{jD\omega_c\frac{n}{F_s}}\, \eta_{l,k,D}^{m',\ddot{m},\dddot{m}}\, \zeta_{l,k,D}^{m',\ddot{m},\dddot{m}}(\tilde{\mathbf{x}}[n]) \tag{2.22}$$

where

$$\mathcal{L} = \{D, D+2, \ldots, H\},$$
$$\mathcal{F} = \{3D+2, 3D+4, \ldots, N\},$$
$$H = \min(3D, N).$$

17
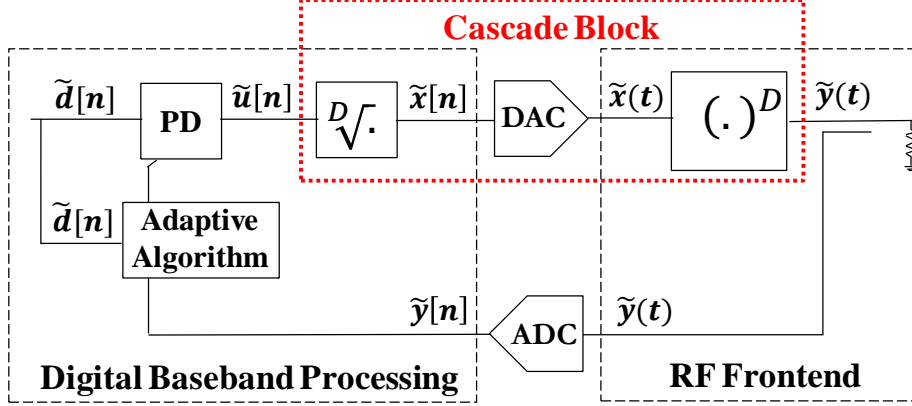
Figure 2.4: Proposed DPD scheme for frequency multiplier based high frequency signal generator block diagram. The Dth root $\sqrt[D]{.}$ is implemented digitally and is ideal while the $(.)^D$ frequency multiplier is non-ideal.

Moreover, note in (2.22) and as mentioned earlier that $k - D$ must be even, which means that $k - 3D$ must be even as well, therefore the summations of k in (2.22) have an increment step of 2. Keeping the terms containing $e^{jD\omega_c \frac{n}{F_s}}$ yields CBBE model for (2.22), given as,

$$\tilde{y}[n] = \sum_{k \in \mathcal{L}} \sum_{l=0}^{\frac{k-D}{2}} \sum_{\substack{m' \in [M] \\ \ddot{m} \in \mathcal{I}_{k'} \\ \dddot{m} \in \mathcal{I}_{D-k'}}} \eta_{l,k,D}^{m',\ddot{m},\dddot{m}} \zeta_{l,k,D}^{m',\ddot{m},\dddot{m}}(\tilde{\mathbf{x}}[n]) + \sum_{k \in \mathcal{F}} \sum_{l=\frac{k-3D}{2}}^{\frac{k-D}{2}} \sum_{\substack{m' \in [M] \\ \ddot{m} \in \mathcal{I}_{k'} \\ \dddot{m} \in \mathcal{I}_{D-k'}}} \eta_{l,k,D}^{m',\ddot{m},\dddot{m}} \zeta_{l,k,D}^{m',\ddot{m},\dddot{m}}(\tilde{\mathbf{x}}[n])$$

(2.23)

2.2.3 Proposed Pruned Digital Predistortion Scheme Formulation

Fig. 2.4 shows the block diagram of the proposed DPD for frequency multipliers. Here, the non-ideal multiplier is cascaded with a $\sqrt[D]{.}$ block (where $\sqrt[D]{.}$ is an ideal D^{th} root block implemented digitally). This cascade represents the nonlinear system that relates $\tilde{u}[n]$ to $\tilde{y}(t)$ to be linearized by the PD block. In the following, the expression of the PD

18

function needed to linearize a non-ideal frequency multiplier, modeled using (2.23), will be developed.

For that, the output signal of the frequency multiplier is first rewritten as the sum of the ideal response and an additive error signal $\tilde{e}(\tilde{\mathbf{x}}[n])$ as,

$$\tilde{y}[n] = G\tilde{x}[n]^D + \tilde{e}(\tilde{\mathbf{x}}[n]),\tag{2.24}$$

where G represents the conversion gain of the frequency multiplier and $\tilde{e}(\tilde{\mathbf{x}}[n])$ takes the form of the frequency multiplier forward model expressed in (2.23). Then, if the PD compensates for the frequency multiplier nonlinearity, $\tilde{y}[n]$ in (2.24) will be equal to the desired signal $\tilde{d}[n]$. Consequently, from (2.24), $\tilde{x}[n]$ can be expressed as a function of the desired and error signals as follows,

$$\tilde{x}[n] = \sqrt[D]{\frac{\tilde{d}[n] - \tilde{e}(\tilde{\mathbf{x}}[n])}{G}} = \sqrt[D]{\frac{\tilde{d}[n] - \tilde{e}\left(\dfrac{\sqrt[D]{\tilde{\mathbf{d}}[n] - \tilde{e}(\tilde{\mathbf{x}}[n])}}{G}\right)}{G}}.\tag{2.25}$$

Approximating $\tilde{e}\left(\sqrt[D]{\dfrac{\tilde{\mathbf{d}}[n] - \tilde{e}(\tilde{\mathbf{x}}[n])}{G}}\right) \approx \tilde{e}\left(\sqrt[D]{\dfrac{\tilde{\mathbf{d}}[n]}{G}}\right)$, (2.25) can be rewritten such that,

$$\tilde{x}[n] \approx \sqrt[D]{\frac{\tilde{d}[n] - \tilde{e}\left(\sqrt[D]{\dfrac{\tilde{\mathbf{d}}[n]}{G}}\right)}{G}}.\tag{2.26}$$

The error signal in (2.26) can be expressed as,

$$\tilde{e}\left(\sqrt[D]{\frac{\tilde{\mathbf{d}}[n]}{G}}\right) = \sum_{k=1}^{|\mathcal{B}|} b_k \tilde{\phi}_k\left(\sqrt[D]{\tilde{\mathbf{d}}[n]}\right),\tag{2.27}$$

where $\tilde{\phi}_k$ are the forward model basis, b_k are the PD coefficients and $\mathcal{B}$ is the set of basis function, $\tilde{\phi}_1, \tilde{\phi}_2, \ldots, \tilde{\phi}_{|\mathcal{B}|}$. Substituting (2.27) in (2.26) and taking (2.26) with equality, we get,

$$\tilde{x}[n] = \sqrt[D]{\frac{\tilde{d}[n] - \sum_{k=1}^{|\mathcal{B}|} b_k \tilde{\phi}_k\left(\sqrt[D]{\tilde{\mathbf{d}}[n]}\right)}{G}}.\tag{2.28}$$

19

It is to note that the expression of $\tilde{x}[n]$ in (2.28) can be rewritten as a function of $\tilde{\mathbf{d}}[n]$ with the definition

$$\tilde{\phi}'_k(\tilde{\mathbf{d}}[n]) := \tilde{\phi}_k\left(\sqrt[D]{\tilde{\mathbf{d}}[n]}\right), \tag{2.29}$$

and where $\tilde{\phi}'_k$ is a PD basis. Consequently, (2.28) becomes,

$$\tilde{x}[n] = \sqrt[D]{\frac{\tilde{d}[n] - \sum_{k=1}^{|\mathcal{B}|} b_k \tilde{\phi}'_k\left(\tilde{\mathbf{d}}[n]\right)}{G}} \tag{2.30}$$

$$= \sqrt[D]{\sum_{k=1}^{|\mathcal{B}|} a_k \tilde{\phi}'_k\left(\tilde{\mathbf{d}}[n]\right)} \tag{2.31}$$

$$= \sqrt[D]{\tilde{u}[n]}, \tag{2.32}$$

where $a_1 = (1 - b_1)/G$ and $a_k = -b_k/G$ for $k \neq 1$ and $\tilde{u}[n] := \sum_{k=1}^{|\mathcal{B}|} a_k \tilde{\phi}'_k\left(\tilde{\mathbf{d}}[n]\right)$.

Now, $\tilde{u}[n]$ can be expressed as a function of the pruned basis in (2.23) as (2.33) below,

$$\tilde{u}[n] = \sum_{k\in\mathcal{L}} \sum_{l=0}^{\frac{k-D}{2}} \sum_{\substack{m'\in[M] \\ \ddot{\boldsymbol{m}}\in\mathcal{I}_{k'} \\ \dddot{\boldsymbol{m}}\in\mathcal{I}_{D-k'}}} \eta'^{\,m',\ddot{\boldsymbol{m}},\dddot{\boldsymbol{m}}}_{l,k,D} \zeta'^{\,m',\ddot{\boldsymbol{m}},\dddot{\boldsymbol{m}}}_{l,k,D}(\tilde{\mathbf{d}}[n]) + \sum_{k\in\mathcal{F}} \sum_{l=\frac{k-3D}{2}}^{\frac{k-D}{2}} \sum_{\substack{m'\in[M] \\ \ddot{\boldsymbol{m}}\in\mathcal{I}_{k'} \\ \dddot{\boldsymbol{m}}\in\mathcal{I}_{D-k'}}} \eta'^{\,m',\ddot{\boldsymbol{m}},\dddot{\boldsymbol{m}}}_{l,k,D} \zeta'^{\,m',\ddot{\boldsymbol{m}},\dddot{\boldsymbol{m}}}_{l,k,D}(\tilde{\mathbf{d}}[n])$$

$$\tag{2.33}$$

where

$$\zeta'^{\,m',\ddot{\boldsymbol{m}},\dddot{\boldsymbol{m}}}_{l,k,D}(\tilde{\mathbf{d}}[n]) = |\tilde{d}[n - m']|^{\frac{2l}{D}} \, \tilde{d}^{\frac{k-D-2l}{D}}[n - m'] \prod_{i=1}^{\frac{k-D}{2}-l} \tilde{d}^{*\frac{1}{D}}[n - \ddot{m}_i] \prod_{j=1}^{D-\frac{k-D}{2}+l} \tilde{d}^{\frac{1}{D}}[n - \dddot{m}_j],$$

and $\eta'^{\,m',\ddot{\boldsymbol{m}},\dddot{\boldsymbol{m}}}_{l,k,D}$ is the PD coefficient. Now, (2.33) is re-written below with separate static basis terms of PD nonlinearity order N' and dynamic basis terms of PD nonlinearity order P'. Note in (2.34), an additional parameter P' is introduced in order to give more flexibility,

so that the nonlinear order of the nonlinear memory basis is limited to P', i.e., $P' \leq N'$.

$$\tilde{u}[n] = \sum_{k \in \mathcal{J}} \sum_{l=0}^{\frac{k-D}{2}} \alpha'_{l,k,D} \, |\tilde{d}[n]|^{\frac{2l}{D}} \, \tilde{d}^{\frac{k-D-2l}{D}}[n] + \sum_{k \in \mathcal{Y}} \sum_{l=\frac{k-3D}{2}}^{\frac{k-D}{2}} \alpha'_{l,k,D} \, |\tilde{d}[n]|^{\frac{2l}{D}} \, \tilde{d}^{\frac{k-D-2l}{D}}[n] \tag{2.34}$$

$$+ \sum_{k \in \mathcal{J}'} \sum_{l=0}^{\frac{k-D}{2}} \sum_{\substack{m' \in [M] \\ \ddot{m} \in \mathcal{I}_{k'} \\ \dddot{m} \in \mathcal{I}_{D-k'} \\ (m',\ddot{m},\dddot{m}) \neq (0,0,0)}} \beta'^{\, m',\ddot{m},\dddot{m}}_{l,k,D} \, \zeta'^{\, m',\ddot{m},\dddot{m}}_{l,k,D}(\tilde{\mathbf{d}}[n]) + \sum_{k \in \mathcal{Y}'} \sum_{l=\frac{k-3D}{2}}^{\frac{k-D}{2}} \sum_{\substack{m' \in [M] \\ \ddot{m} \in \mathcal{I}_{k'} \\ \dddot{m} \in \mathcal{I}_{D-k'} \\ (m',\ddot{m},\dddot{m}) \neq (0,0,0)}} \beta'^{\, m',\ddot{m},\dddot{m}}_{l,k,D} \, \zeta'^{\, m',\ddot{m},\dddot{m}}_{l,k,D}(\tilde{\mathbf{d}}[n]),$$

where

$$\mathcal{J} = \{D, D+2, \ldots, H'\},$$
$$\mathcal{Y} = \{3D+2, 3D+4, \ldots, N'\},$$
$$H' = \min(3D, N'),$$
$$\mathcal{J}' = \{D, D+2, \ldots, H''\},$$
$$\mathcal{Y}' = \{3D+2, 3D+4, \ldots, P'\},$$
$$H'' = \min(3D, P'),$$

α'_i and $\beta'^{\, m',\ddot{m},\dddot{m}}_{l,k,D}$ are the static and dynamic PD coefficients, respectively.

Because of the BW expansion due to nonlinearities of the cascade system, the sampling rate F_s is set to capture all spectral regrowth as compared to the original signal Nyquist rate. One observes that due to this high sampling rate, some terms of (2.34) are almost redundant. For example, one expects

$$\tilde{d}[n]\tilde{d}^*[n-m] \cong |\tilde{d}[n]|^2, \quad \text{for} \quad m < S_T, \tag{2.35}$$

and

$$\tilde{d}[n]\tilde{d}[n-m] \cong \tilde{d}[n]^2, \quad \text{for} \quad m < S_T. \tag{2.36}$$

However, this approximation does not hold for terms that differ by a sufficient time lag, i.e.,

$$\tilde{d}[n]\tilde{d}^*[n-m] \ncong |\tilde{d}[n]|^2, \quad \text{for} \quad m > S_T, \tag{2.37}$$

21

where S_T is appropriately chosen. This has motivated the introduction of an integer Memory Step parameter S that can be used to generate high memory depth terms, where $S > 0$ designates the sample step separating two consecutive samples of $\tilde{d}[n]$. This idea was previously highlighted by [39], where it was demonstrated that S can be found by systematic or empirical methods and showed similar linearization performance in both methods. We chose the less complicated empirical way as S has then to be determined only once and remains constant during DPD iterations. Therefore, (2.34) becomes,

$$\tilde{u}[n] = \sum_{k \in \mathcal{J}} \sum_{l=0}^{\frac{k-D}{2}} \alpha'_{l,k,D} \, |\tilde{d}[n]|^{\frac{2l}{D}} \, \tilde{d}^{\frac{k-D-2l}{D}}[n] + \sum_{k \in \mathcal{Y}} \sum_{l=\frac{k-3D}{2}}^{\frac{k-D}{2}} \alpha'_{l,k,D} \, |\tilde{d}[n]|^{\frac{2l}{D}} \, \tilde{d}^{\frac{k-D-2l}{D}}[n] \qquad (2.38)$$

$$+ \sum_{k \in \mathcal{J}'} \sum_{l=0}^{\frac{k-D}{2}} \sum_{\substack{m' \in [M]^S \\ \ddot{m} \in \mathcal{I}^S_{k'} \\ \dddot{m} \in \mathcal{I}^S_{D-k'} \\ (m',\ddot{m},\dddot{m}) \neq (0,\mathbf{0},\mathbf{0})}} \beta'^{\,m',\ddot{m},\dddot{m}}_{l,k,D} \, \zeta'^{\,m',\ddot{m},\dddot{m}}_{l,k,D}(\tilde{\mathbf{d}}[n]) + \sum_{k \in \mathcal{Y}'} \sum_{l=\frac{k-3D}{2}}^{\frac{k-D}{2}} \sum_{\substack{m' \in [M]^S \\ \ddot{m} \in \mathcal{I}^S_{k'} \\ \dddot{m} \in \mathcal{I}^S_{D-k'} \\ (m',\ddot{m},\dddot{m}) \neq (0,\mathbf{0},\mathbf{0})}} \beta'^{\,m',\ddot{m},\dddot{m}}_{l,k,D} \, \zeta'^{\,m',\ddot{m},\dddot{m}}_{l,k,D}(\tilde{\mathbf{d}}[n])$$

where

$$\mathcal{I}^S_p = \Big\{ \mathbf{q} \in \mathcal{I}_p \;\Big|\; S|q_1, \dots, S|q_p \Big\},$$
$$[M]^S = \{0, S, 2S, 3S, \dots, \lfloor M/S \rfloor \cdot S\},$$

and recall that $a|b$ indicates that the integer a divides the integer b. Note above that for the special case of $S = 1$, (2.34) and (2.38) are equivalent. The effect of the pruning strategy, described in the theory above on the number of coefficients is highlighted in Table 2.1 where the the proposed DPD is compared to the full CBBE Volterra series for $D = 2$ and different values of M and S.

Table 2.1: Different DPD schemes with number of coefficients

DPD Scheme	N'	M	P'	S	# Coeff
Full Volterra	10	10	-	1	3215
Full Volterra	10	2	-	1	756
Proposed (Config 1)	10	2	4	1	39
Proposed (Config 2)	10	10	4	5	39
Proposed (Config 3)	10	10	4	1	1895

2.2.4 Proposed Generalized Digital Predistortion Scheme Formulation

If one uses the discrete-time Volterra series based expression of a frequency multiplier from [1], re-written below,

$$\tilde{y}(n) = \sum_{k=0}^{N-D} \sum_{\ell_1^k \in \mathcal{I}_k} \sum_{\ell_{k+1}^{2k+D} \in \mathcal{I}_{k+D}} \tilde{f}\left(\ell_1^{2k+D}\right) \prod_{i=1}^{k} \tilde{x}^*[n-\ell_i] \prod_{j=k+1}^{2k+D} \tilde{x}[n-\ell_j], \qquad (2.39)$$

where $\tilde{f}\left(\ell_1^{2k+D}\right)$ are the Volterra kernels, $\ell_1^{2k+D} = [\ell_1, \ldots, \ell_{2k+D}]^T$ and using (2.29) and (2.32), the predistorted signal, $\tilde{u}[n]$, can then be expressed as follows,

$$\tilde{u}(n) = \sum_{k=0}^{D(N'-1)} \sum_{\ell_1^k \in \mathcal{I}_k} \sum_{\ell_{k+1}^{2k+D} \in \mathcal{I}_{k+D}} \tilde{f}'\left(\ell_1^{2k+D}\right) \prod_{i=1}^{k} \tilde{d}^{*\frac{1}{D}}[n-\ell_i] \prod_{j=k+1}^{2k+D} \tilde{d}^{\frac{1}{D}}[n-\ell_j], \qquad (2.40)$$

where $\tilde{f}'\left(\ell_1^{2k+D}\right) \in \mathcal{B}$ and $\mathcal{B}$ is the set of basis functions.

2.2.5 Comparison Among Proposed and Previous DPD Schemes

Tables 2.2 – 2.5 list the DPD basis for a frequency doubler ($D = 2$) and quadrupler ($D = 4$) using DPD scheme of [36], [1] and the proposed work for $N'/D = 2$, $N'/D = 4$ and $N'/D = 5$ respectively. Tables 2.2 – 2.5 show that, unlike the proposed work, the DPD basis of [36] and [1] are independent of the value D. It also shows that the previous DPD

Table 2.2: Different DPD schemes with their basis for $N'/D = 2$

	$M = 1, M_{L3} = 1, M_{NL3} = 1$
DPD scheme of [36]	$d[n], d[n-1], d[n]|d[n]|, d[n]|d[n-1]|,$ $d[n-1]|d[n]|, d[n-1]|d[n-1]|$
DPD scheme of [1]	$d[n], d[n-1], d[n]|d[n]|, d[n]|d[n]|^2$
Proposed DPD scheme $(D = 2)$	$d[n], d[n-1], d^{\frac{1}{2}}[n]d^{\frac{1}{2}}[n-1], d^{\frac{3}{2}}[n]d^{*\frac{1}{2}}[n-1], d^{\frac{3}{2}}[n-1]d^{*\frac{1}{2}}[n],$ $d[n]|d[n]|, d[n]|d[n-1]|, d[n-1]|d[n]|, d[n-1]|d[n-1]|,$ $d^{\frac{1}{2}}[n]d^{\frac{1}{2}}[n-1]|d[n]|, d^{\frac{1}{2}}[n]d^{\frac{1}{2}}[n-1]|d[n-1]|$
Proposed DPD scheme $(D = 4)$	$d[n], d[n-1], d^{\frac{1}{2}}[n]d^{\frac{1}{2}}[n-1], d^{\frac{3}{4}}[n]d^{\frac{1}{4}}[n-1], d^{\frac{1}{4}}[n]d^{\frac{3}{4}}[n-1]$

schemes are missing the fractional power and conjugate basis, which can be seen in the unpruned and pruned PD basis proposed in this work. It is also to note that the fractional power basis in (2.34) and (2.40) can be approximated using Taylor series expansion. In that case, although increasing the nonlinearity order in [36] and [1] can model the missing fractional power basis, the conjugate basis are still missing.

Table 2.3: Different DPD schemes with their basis for $N'/D = 4$

$M = 1, M_{L3} = 1, M_{NL3} = 1$	
DPD scheme of [36]	$d[n], d[n-1], d[n]\|d[n]\|, d[n]\|d[n-1]\|, d[n-1]\|d[n]\|,$ $d[n-1]\|d[n-1]\|, d[n]\|d[n]\|^2, d[n]\|d[n-1]\|^2,$ $d[n-1]\|d[n-1]\|^2, d[n-1]\|d[n]\|^2, d[n-1]\|d[n]\|^3,$ $d[n]\|d[n-1]\|^3, d[n]\|d[n]\|^3, d[n-1]\|d[n-1]\|^3$
DPD scheme of [1]	$d[n], d[n-1], d[n]\|d[n]\|, d[n]\|d[n-1]\|, d[n-1]\|d[n]\|,$ $d[n]\|d[n]\|^2, d[n]\|d[n-1]\|^2, d[n-1]\|d[n-1]\|^2,$ $d[n-1]\|d[n]\|^2, d[n-1]\|d[n]\|\|d[n-1]\|, d[n]\|d[n]\|\|d[n-1]\|,$ $d[n]\|d[n]\|^3, d[n]\|d[n-1]\|^3, d[n]\|d[n]\|^4$
Proposed DPD scheme ($D = 2$)	$d[n], d[n-1], d^{\frac{1}{2}}[n]d^{\frac{1}{2}}[n-1], d^{\frac{3}{2}}[n]d^{*\frac{1}{2}}[n-1],$ $d^{\frac{3}{2}}[n-1]d^{*\frac{1}{2}}[n], d[n]\|d[n]\|, d[n]\|d[n-1]\|, d[n-1]\|d[n]\|,$ $d[n-1]\|d[n-1]\|, d^{\frac{1}{2}}[n]d^{\frac{1}{2}}[n-1]\|d[n]\|,$ $d^{\frac{1}{2}}[n]d^{\frac{1}{2}}[n-1]\|d[n-1]\|, d[n]\|d[n]\|^2, d[n]\|d[n]\|^3$
Proposed DPD scheme ($D = 4$)	$d[n], d[n-1], d^{\frac{1}{2}}[n]d^{\frac{1}{2}}[n-1], d^{\frac{3}{4}}[n]d^{\frac{1}{4}}[n-1],$ $d^{\frac{1}{4}}[n]d^{\frac{3}{4}}[n-1], d[n]\|d[n]\|, d[n]\|d[n]\|^{\frac{1}{2}}$

Table 2.4: Previous DPD schemes with their basis for $N'/D = 5$

$M = 2, M_{L3} = 2, M_{NL3} = 2$	
DPD scheme of [36]	$d[n], d[n-1], d[n-2], d[n]\|d[n]\|, d[n]\|d[n-1]\|, d[n]\|d[n-2]\|,$ $d[n-1]\|d[n]\|, d[n-1]\|d[n-1]\|, d[n-1]\|d[n-2]\|, d[n-2]\|d[n]\|,$ $d[n-2]\|d[n-1]\|, d[n-2]\|d[n-2]\|, d[n]\|d[n]\|^2, d[n]\|d[n-1]\|^2,$ $d[n]\|d[n-2]\|^2, d[n-1]\|d[n]\|^2, d[n-1]\|d[n-1]\|^2, d[n-1]\|d[n-2]\|^2,$ $d[n-2]\|d[n]\|^2, d[n-2]\|d[n-1]\|^2, d[n-2]\|d[n-2]\|^2, d[n]\|d[n]\|^3,$ $d[n]\|d[n-1]\|^3, d[n]\|d[n-2]\|^3, d[n-1]\|d[n]\|^3, d[n-1]\|d[n-1]\|^3,$ $d[n-1]\|d[n-2]\|^3, d[n-2]\|d[n]\|^3, d[n-2]\|d[n-1]\|^3,$ $d[n-2]\|d[n-2]\|^3, d[n]\|d[n]\|^4, d[n]\|d[n-1]\|^4, d[n]\|d[n-2]\|^4,$ $d[n-1]\|d[n]\|^4, d[n-1]\|d[n-1]\|^4, d[n-1]\|d[n-2]\|^4,$ $d[n-2]\|d[n]\|^4, d[n-2]\|d[n-1]\|^4, d[n-2]\|d[n-2]\|^4$
DPD scheme of [1]	$d[n], d[n]\|d[n]\|, d[n]\|d[n]\|^2,$ $d[n]\|d[n]\|^3, d[n]\|d[n]\|^4, d[n]\|d[n]\|^5, d[n-1], d[n-2],$ $d[n]\|d[n-1]\|, d[n]\|d[n-1]\|^2, d[n]\|d[n-1]\|^3, d[n]\|d[n-2]\|,$ $d[n]\|d[n-2]\|^2, d[n]\|d[n]\|\|d[n-1]\|,$ $d[n]\|d[n]\|\|d[n-1]\|^2, d[n]\|d[n]\|\|d[n-2]\|,$ $d[n]\|d[n]\|^2\|d[n-1]\|, d[n]\|d[n-1]\|,$ $\|d[n]\|d[n-1]\|d[n-1]\|, \|d[n]\|d[n-1]\|d[n-1]\|^2,$ $\|d[n]\|d[n-2]\|, \|d[n]\|d[n-2]\|d[n-2]\|,$ $\|d[n]\|^2 d[n-1], \|d[n]\|^2 d[n-1]\|d[n-1]\|,$ $\|d[n]\|^2 d[n-2], \|d[n]\|^3 d[n-1], d[n-1]\|d[n]\|,$ $d[n-1]\|d[n]\|^2, d[n-1]\|d[n]\|^4, d[n-2]\|d[n]\|, d[n-1]\|d[n]\|^3$

26

Table 2.5: Proposed DPD schemes with their basis for $N'/D = 5$

$M = 2, P'/D = 2, S = 1$	
Proposed DPD scheme ($D = 2$)	$d[n], d[n]\|d[n]\|, d[n]\|d[n]\|^2, d[n]\|d[n]\|^3,$ $d[n]\|d[n]\|^4, d[n-1], d[n-1]\|d[n-1]\|, d[n-2],$ $d[n-2]\|d[n-2]\|, d^{\frac{1}{2}}[n-1]d^{\frac{1}{2}}[n]\|d[n]\|, d^{\frac{1}{2}}[n-1]d^{\frac{1}{2}}[n]\|d[n-1]\|,$ $d^{\frac{1}{2}}[n-1]d^{\frac{1}{2}}[n]\|d[n-2]\|,$ $d^{\frac{1}{2}}[n-2]d^{\frac{1}{2}}[n]\|d[n]\|, d^{\frac{1}{2}}[n-2]d^{\frac{1}{2}}[n]\|d[n-1]\|,$ $d^{\frac{1}{2}}[n-2]d^{\frac{1}{2}}[n]\|d[n-2]\|, d^{\frac{1}{2}}[n]d^{\frac{1}{2}}[n]\|d[n-1]\|,$ $d^{\frac{1}{2}}[n]d^{\frac{1}{2}}[n]\|d^{[}n-2]\|, d^{\frac{1}{2}}[n-1]d^{\frac{1}{2}}[n-1]\|d^{[}n]\|,$ $d^{\frac{1}{2}}[n-1]d^{\frac{1}{2}}[n-1]\|d[n-2]\|, d^{\frac{1}{2}}[n-2]d^{\frac{1}{2}}[n-2]\|d^{[}n]\|,$ $d^{\frac{1}{2}}[n-2]d^{\frac{1}{2}}[n-2]\|d[n-1]\|, d^{\frac{1}{2}}[n-2]d^{\frac{1}{2}}[n]\|d[n]\|,$ $d^{\frac{1}{2}}[n-2]d^{\frac{1}{2}}[n]\|d[n-1]\|, d^{\frac{1}{2}}[n-2]d^{\frac{1}{2}}[n]\|d[n-2]\|,$ $d^{\frac{1}{2}}[n-1]d^{\frac{1}{2}}[n], d^{\frac{1}{2}}[n-2]d^{\frac{1}{2}}[n-1],$ $d^{\frac{1}{2}}[n-2]d^{\frac{1}{2}}[n], d^{\frac{1}{2}}[n]d^{*\frac{1}{2}}[n-1]d[n],$ $d^{\frac{1}{2}}[n]d^{*\frac{1}{2}}[n-1]d[n-2], d^{\frac{1}{2}}[n]d^{*\frac{1}{2}}[n-2]d[n], d^{\frac{1}{2}}[n]d^{*\frac{1}{2}}[n-2]d[n-1],$ $d^{\frac{1}{2}}[n-1]d^{*\frac{1}{2}}[n]d[n-1], d^{\frac{1}{2}}[n-1]d^{*\frac{1}{2}}[n]d[n-2],$ $d^{\frac{1}{2}}[n-1]d^{*\frac{1}{2}}[n-2]d[n], d^{\frac{1}{2}}[n-1]d^{*\frac{1}{2}}[n-2]d[n-1],$ $d^{\frac{1}{2}}[n-2]d^{*\frac{1}{2}}[n]d[n-1], d^{\frac{1}{2}}[n-2]d^{*\frac{1}{2}}[n]d[n-2],$ $d^{\frac{1}{2}}[n-2]d^{*\frac{1}{2}}[n-1]d[n],$ $d^{\frac{1}{2}}[n-2]d^{*\frac{1}{2}}[n-1]d[n-2]$
Proposed DPD scheme ($D = 4$)	$d[n], d[n]\|d[n]\|, d[n]\|d[n]\|^{\frac{1}{2}}, d[n]\|d[n]\|^{\frac{6}{4}}, d[n-1], d[n-2],$ $d^{\frac{3}{4}}[n]d^{\frac{1}{4}}[n-1], d^{\frac{3}{4}}[n]d[n-2],$ $d^{\frac{3}{4}}[n]d^{\frac{1}{4}}[n-1], d^{\frac{1}{2}}[n]d^{\frac{1}{2}}[n-1],$ $d^{\frac{1}{2}}[n]d[n-1]d[n-2], d^{\frac{1}{2}}[n]d^{\frac{1}{2}}[n-2], d^{\frac{1}{4}}[n]d^{\frac{3}{4}}[n-1],$ $d^{\frac{1}{4}}[n]d^{\frac{1}{2}}[n-1]d^{\frac{1}{4}}[n-2],$ $d^{\frac{1}{4}}[n-1]d^{\frac{3}{4}}[n-2]d^{\frac{1}{4}}[n]d^{\frac{1}{4}}[n-1]d^{\frac{1}{2}}[n-2],$ $d^{\frac{1}{4}}[n]d^{\frac{3}{4}}[n-2],$ $d^{\frac{1}{4}}[n-1]d^{\frac{1}{2}}[n-2], d^{\frac{3}{4}}[n-1]d[n-2], d^{\frac{1}{2}}[n-1]d^{\frac{1}{2}}[n-2]$

2.2.6 Proposed DPD Training

The objective of DPD is to minimize the error between the DPD input signal $\tilde{d}[n]$ and the received signal $\tilde{y}[n]$, where $\tilde{y}[n]$ is the feedback signal, obtained at the output of nonlinear system and DPD has to compensate for its nonlinearity. In the proposed DPD training, the quadratic cost function

$$J(\mathbf{a}) = \sum_{n=M+1}^{L} \left(\frac{\tilde{y}[n]}{G} - \tilde{d}[n] \right) \left(\frac{\tilde{y}[n]}{G} - \tilde{d}[n] \right)^*, \tag{2.41}$$

is adopted, where L is the length of the training data that is used in (2.41), G is the desired gain and $\mathbf{a}$ is the vector of DPD coefficients that are to be optimized to minimize the cost function J. Using (2.30), (2.31) and the direct learning algorithm, appeared first in [40, 41], the optimal choice of $\mathbf{a}$ is iteratively calculated and the coefficients are obtained by the update equation,

$$\mathbf{a}_{k+1} = \mathbf{a}_k - \tau (\mathbf{\Phi'}^H \mathbf{\Phi'})^{-1} \mathbf{\Phi'}^H \left(\frac{\overline{\mathbf{y}}}{G} - \overline{\mathbf{d}} \right), \tag{2.42}$$

where $\mathbf{a}_k$ are the kth iteration DPD coefficients,

$$\mathbf{\Phi'} = \begin{bmatrix} \phi'_1(\tilde{\mathbf{d}}[M+1]) & \phi'_2(\tilde{\mathbf{d}}[M+1]) & \dots & \phi'_{|\mathcal{B}|}(\tilde{\mathbf{d}}[M+1]) \\ \phi'_1(\tilde{\mathbf{d}}[M+2]) & \dots & \dots & \phi'_{|\mathcal{B}|}(\tilde{\mathbf{d}}[M+2]) \\ \vdots & \vdots & \vdots & \vdots \\ \phi'_1(\tilde{\mathbf{d}}[L]) & \phi'_2(\tilde{\mathbf{d}}[L]) & \dots & \phi'_{|\mathcal{B}|}(\tilde{\mathbf{d}}[L]) \end{bmatrix},$$

$\overline{\mathbf{y}} = (\tilde{y}[M+1], \tilde{y}[M+2], \dots, \tilde{y}[L])^T$, $\overline{\mathbf{d}} = (\tilde{d}[M+1], \tilde{d}[M+2], \dots, \tilde{d}[L])^T$ and $\tau > 0$ is the update step size.

2.2.7 PAPR Reduction

One of the interesting feature of applying DPD to frequency multipliers is the PAPR reduction of the input signal. This is in contrast to the case of PA linearization, where the predistorted signal at the input of the frequency multiplier has higher PAPR than that of
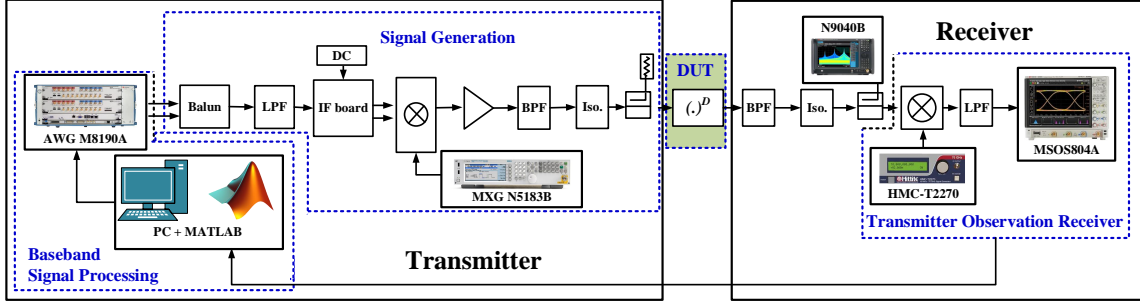
Figure 2.5: Block diagram of the test setup.

the original input signal. For example, it will be showed in the experiment validation later that when starting with a test signal with PAPR equal to 11 dB, application of the DPD function yielded a PAPR equal to 3.5-4.5 dB. This significant reduction of the PAPR would relax, i) the digital-to-analog converter (DAC) requirements and ii) makes it possible to overdrive the frequency multiplier. It is to note that, unlike PAs, a higher conversion gain can be extracted from a frequency multiplier with higher input drive level. This is due to the nature of operation of the frequency multipliers.

2.3 Experimental Validation

2.3.1 Measurement setup

Fig. 2.5 shows the measurement setup used to validate the proposed DPD scheme. Four different frequency multipliers were used in these experiments; i) a frequency doubler with output centered at 25 GHz, ii) a different frequency doubler with output centered at 28 GHz, iii) a frequency tripler with output centered at 63 GHz and, iv) a frequency quadrupler with output centered at 25 GHz. The vector modulated test signals are generated using a 12 bit, 12 GS/s arbitrary wave generator (AWG) (M8190A from Keysight Technologies) and
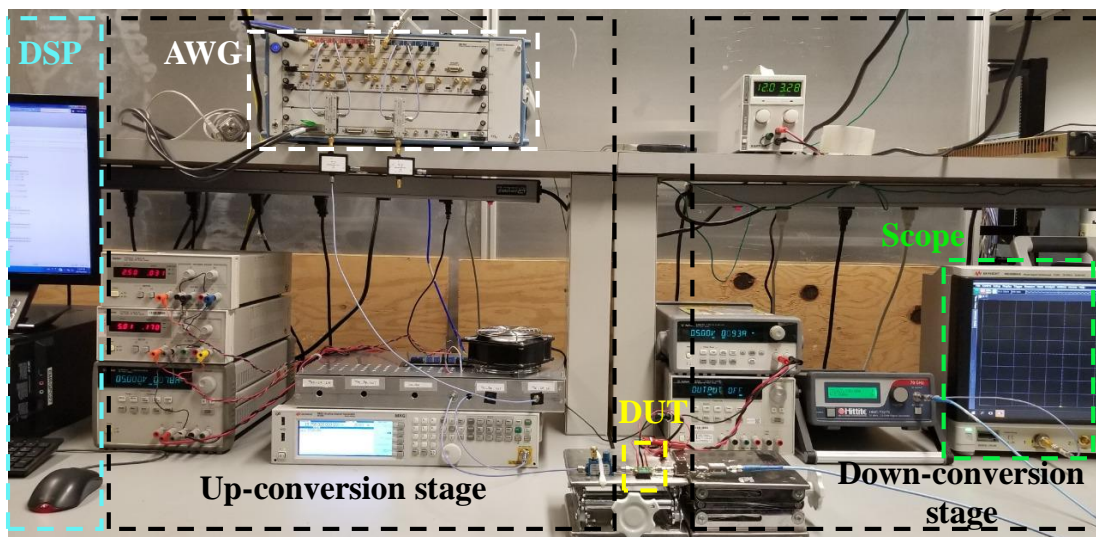
Figure 2.6: Photograph of the test setup.

are centered at an IF of 1.75 GHz. A custom built IF board containing a hybrid 90° coupler is then used to convert the IF signal into in-phase and quadrature signal components so that an IQ mixer can be used later to up-convert the IF signal with good image rejection. Two LO sources (MXG-N5183B from Keysight Technologies and HMC-T2270 from Hittite Microwave) are used to drive the upconversion and downconversion mixers used in the setup. Dedicated upconverters and downconverters are used in all four test conditions.

For frequency doubler based TX architectures, two frequency doublers are used to evaluate the robustness of the DPD scheme on different technologies. The doublers used are A2510-2x-20 (from Spacek Labs) and HMC578 (from Analog Devices) to upconvert the signals to 25 GHz and 28 GHz, respectively. In the TX chain, an IQ mixer (MMIQ 1037H from Marki Microwave) is used to upconvert the IF signal to 12.5 GHz for the first frequency doubler and 14 GHz for the second frequency doubler case. The signal is then amplified using a gain amplifier (MAAM-011109 from MACOM). Afterwards, a low pass filter (LPF) (FLP-1250 from Marki Microwave) is used to reject the residual image and LO leakage.

For the frequency quadrupler based TX architecture, an IQ mixer (MLIQ 0416L from

30

Marki Microwave) is used to upconvert the IF signal to 6.25 GHz. The signal is then amplified by a gain amplifier (MAAM-011109 from MACOM) followed by a LPF (VLF-7200+ from Mini Circuits) and a directional coupler (1851 from Krytar). Then, a cascade of two doublers (HMC573 from Analog Devices followed by A2510-2x-20 from SpaceK Labs) are used to first upconvert the signal to 12.5 GHz and then to 25 GHz, and act as a frequency quadrupler.

In both doubler and quadrupler cases, a directional coupler (110040010K from Krytar) is used to observe and/or capture the RF signal via spectrum analyzer (N9040B from Keysight Technologies). Afterwards, a downconversion mixer (MM1-1140H from Marki Microwave) is used to convert the RF signal to IF.

For the frequency tripler measurement setup, an IQ mixer (MLIQ-1037H from Marki Microwave) is used to upconvert the IF test signal to 21 GHz. The signal is then amplified by a cascade of two gain amplifiers (MAAM-011109 from MACOM and HMC698 from Analog Devices) and filtered through a band pass filter (BPF) (FB-2020 from Marki Microwave), followed by a directional coupler (110040010K from Krytar). The frequency tripler (WR12x3 from Virginia Diodes) outputs the signal at 63 GHz and feeds a custom built waveguide BPF, an amplifier (QGW-50661720 from Quinstar) and a balanced mixer (SFB-15-N1-M from Sage Millimeter). The balanced mixer downconverts the RF signal (63 GHz) to IF (3.0275 GHz). The LO signal passes through a gain amplifier (QGW-50661720 from Quinstar) and custom built BPF before it is fed to the mixer.

After down-conversion of the frequency multiplier output signals, the resulting IF signals are captured and digitized using a 20 GS/s, 10-bit, 8 GHz analog BW oscilloscope (MSOS804A from Keysight Technologies) for DPD training. All the signal processing is done in MATLAB software.

The measurements are performed using 100 MHz, 200 MHz and 400 MHz modulation BW OFDM signals with 120 kHz sub-carrier spacing and 11 dB PAPR. The 100 MHz, 200 MHz and 400 MHz test signals are sampled at 1 GS/s, 2 GS/s, and 3 GS/s, with their sub-carriers modulated using 64-QAM, 256-QAM and 256-QAM symbols, respectively.

In the measurement tests of all frequency multipliers, five cases are validated, namely, a) only D^{th} root applied, b) memoryless DPD of [1] applied, c) memoryless proposed DPD

applied, d) DPD of [1] applied and, e) proposed DPD applied. All these five cases of interest are tested in order to make a comparison and show the ACPR and EVM improvement compared to the DPD of [1]. The PAPR of the predistorted signal in case (a) is 5.5 dB while it is 3.5-4.5 dB in cases (b)-(e) depending upon the input drive level to the frequency multiplier.

Tables 2.6 – 2.9 present a summary of the measurement results where the settings of the various DPD cases are designated using triples and 4-tuples. Specifically, for (b) and (d), the 4-tuple $(N_1, N_3, M_{L3}, M_{NL3})$ indicates the maximum nonlinearity order of static basis (N_1), maximum nonlinearity order of memory basis (N_3), linear memory depth (M_{L3}) and nonlinear memory depth (M_{NL3}). For cases (c) and (e), the triple indicates (N', M, P').

Before discussing the measurement results, we clarify the definition of EVM used in this work. After removal of the cyclic prefix, the discrete Fourier transform (DFT) of the discrete time aligned input signal $\tilde{d}[n]$ and the sampled received signal $\tilde{y}[n]$ of length L is given as $\tilde{y}_{\text{FFT}}[v]$ and $\tilde{d}_{\text{FFT}}[v]$, respectively. The EVM per OFDM symbol is defined as,

$$\text{EVM} = \frac{\sum_{j=0}^{L_{\text{D}}} |\tilde{y}_{\text{FFT}}[v(j)]B[v(j)] - \tilde{d}_{\text{FFT}}[v(j)]|^2}{\sum_{j=0}^{L_{\text{D}}} |\tilde{d}_{\text{FFT}}[v(j)]|^2}, \tag{2.43}$$

where L_{D} is the total number of data sub-carriers, $v(j)$ is the index of the DFT corresponding to the jth data sub-carrier, and $B[v]$ is the transfer function of a linear equalization filter derived from L_{P} OFDM pilot sub-carriers, where L_{P} is the total number of pilot sub-carriers.

2.3.2   Linearization of Frequency Doubler

Table 2.6 summarizes the results for the first frequency doubler with 100 MHz, 200 MHz and 400 MHz test signals. It can be concluded from these that applying only a Dth root (case (a)) is insufficient to ensure acceptable output signal quality. To correct for the residual distortion, the DPDs of case (b) with 9 coefficients, case (c) with 5 coefficients, case (d) with 34 coefficients and case (e) with 39 coefficients are applied. The memory step was set to $S = 1$ for the cases (b) – (d) and $S = 5$ or $S = 7$ for case (e).

Table 2.6: Linearization results for a frequency doubler (Spacek Labs) centered at 25 GHz

			Only static		With memory	
		(a)	(b)	(c)	(d)	(e)
BW: 100 MHz	Settings	-	(4,5,0,0)	(10,0,-)	(4,5,2,2)	(10,10,4)
	S	-	1	1	1	5
	# Coeff	-	9	5	34	39
	ACPR L/U (dB)	26 / 26	49 / 48	49 / 48	51 / 51	55 / 55
	EVM (%)	12.2	1	1	0.7	0.5
BW: 200 MHz	Settings	-	(4,5,0,0)	(10,0,-)	(4,5,2,2)	(10,10,4)
	S	-	1	1	1	5
	# Coeff	-	9	5	34	39
	ACPR L/U (dB)	26 / 26	46 / 42	46 / 42	47 / 44	50 / 49
	EVM (%)	12.7	2.2	2.1	1.6	0.9
BW: 400 MHz	Settings	-	(4,5,0,0)	(10,0,-)	(4,5,2,2)	(10,14,4)
	S	-	1	1	1	7
	# Coeff	-	9	5	34	39
	ACPR L/U (dB)	26 / 26	43 / 43	43 / 44	44 / 43	48 / 49
	EVM (%)	12	2.8	2.9	2.6	1.3
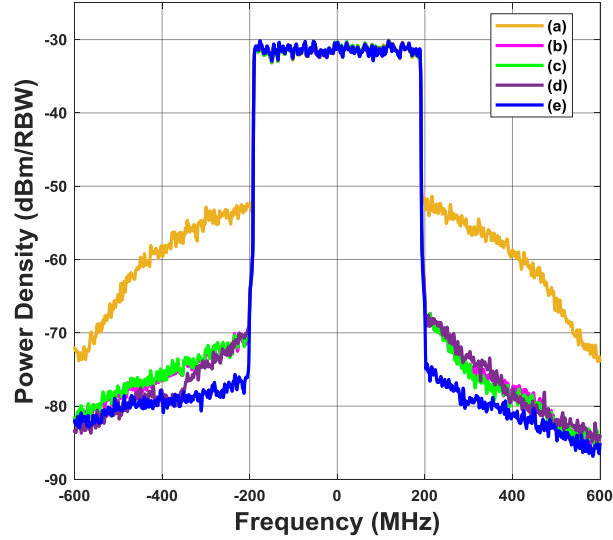
Figure 2.7: Measured output spectra of frequency doubler (SpaceK Labs) driven with OFDM signal of modulation BW 400 MHz: (a) After only square root applied; (b) After memoryless DPD of [1] applied; (c) After memoryless proposed DPD applied; (d) After DPD of [1] applied; (e) After proposed DPD applied.
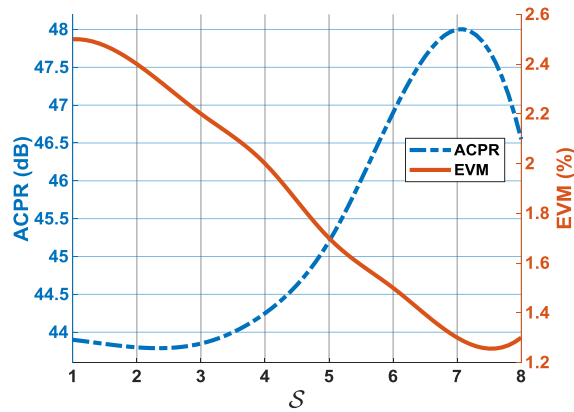
Figure 2.8: Measured ACPR and EVM results of the frequency doubler (from SpaceK Labs) with modulation BW 400 MHz versus different S (step) values. Here, ACPR indicates the average ACPR value of lower and upper ACPR values.
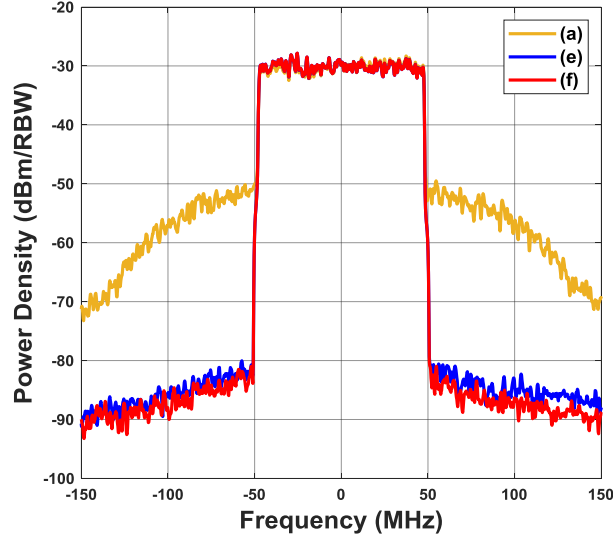
Figure 2.9: Measured output spectra of frequency doubler (SpaceK Labs) driven with OFDM signal of modulation BW 100 MHz: (a) After only square root applied; (e) After proposed DPD (with 39 coefficients) applied; (f) After proposed DPD (with 1895 coefficients) applied.

Table 2.7: Linearization results for a frequency doubler (HMC578) centered at 28 GHz

	Signal BW: 100 MHz		Signal BW: 200 MHz		Signal BW: 400 MHz	
	(a)	(e)	(a)	(e)	(a)	(e)
Settings	-	(20,12,4)	-	(20,14,4)	-	(20,8,4)
S	-	6	-	7	-	4
# Coeff	-	44	-	44	-	44
ACPR (dB)	22 / 22	54/ 54	21 / 21	51/51	21/ 21	47/ 46
EVM (%)	20.2	0.8	22.7	0.8	21.7	1.8
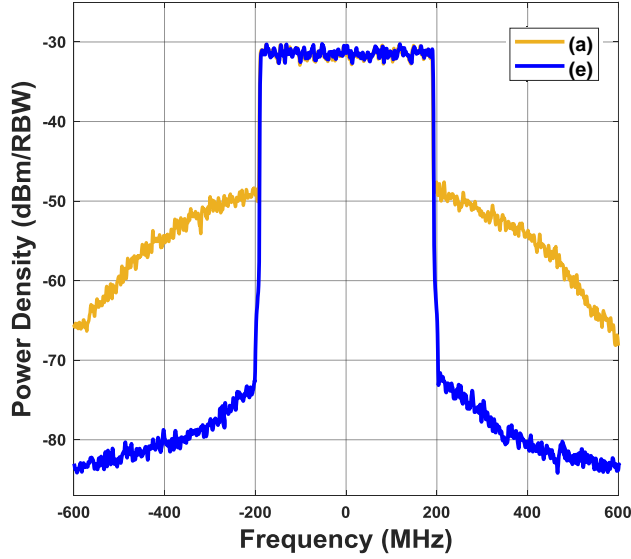
Figure 2.10: Measured output spectra of frequency doubler (HMC578) driven with OFDM signal of modulation BW 400 MHz: (a) After only square root applied; (e) After proposed DPD applied.

Based on Table 2.6, both memoryless DPD cases showed some improvement of the ACPR and EVM to between 43 – 48 dB and 2.9 – 1.0% compared to 26 dB and 12% for the case of Dth root DPD. Of particular note, was the very limited improvement in EVM and ACPR in the case of the 400 MHz test signal. While further improvement was achieved using the DPD of case (d) for the 100 MHz test signal, only marginal improvements were observed for the 400 MHz test signal. Finally, with the proposed DPD of case (e), the ACPR and EVM for the 400 MHz signal were improved from 26 dB and 12% to 48 dB and 1.3% respectively. Fig. 2.7 shows the output spectrum corresponding to the five DPD cases for the 400 MHz test signal.

To demonstrate the importance of the memory step S on the linearization capacity of the proposed DPD scheme, Fig. 2.8 shows the EVM and ACPR versus the memory step where the number of coefficients was fixed to 39 for the 400 MHz test signal. Based on the figure, there is an optimal memory step $S = 7$ where ACPR is maximized and EVM is minimized. Furthermore, the measurement results in Fig. 2.9 shows a comparison between the results depicted in Table 2.6 case (e) and case (f) where the memory step is changed to $S = 1$ and the memory depth is kept constant at $M = 10$. This resulted in an increase

36

of the number of coefficients from 39 to 1895 as shown in Table 2.1. One would expect a significant improvement in the ACPR and EVM results due to huge difference in the number of coefficients in the two cases. However, the ACPR was only slightly increased from 55 to 57 dB while EVM was maintained at 0.5%. It is to note that increasing the value of memory step S from 1 to 5 allowed to increase the memory depth M from 2 to 10 without exploding the number of coefficients while achieving excellent results.

To verify the generality of the proposed DPD scheme for frequency doublers, a second doubler (HMC578 from Analog Devices) driven in higher compression, i.e., worse starting ACPR and EVM, was used as DUT. Because this second DUT is driven further into nonlinearity, the PD nonlinearity order N' is increased from 10 to 20, resulting in a number of coefficients increase from 39 to 44. Like the first frequency doubler case, excellent linearization results were obtained, as shown in Table 2.7 and Fig. 2.10.

2.3.3 Linearization of Frequency Tripler

The linearization results obtained using the frequency tripler are summarized in Table 2.8. Based on these results, the application of the cubic root function (case(a)) was insufficient to linearize the tripler response and significant residual out-of-band distortions were observed. To correct for the residual distortion, the DPDs of cases (b)-(e) are applied. As in the case of the frequency doublers, the memoryless DPD showed limited linearization performance as the EVM and ACPR improved only to 4.4% and 33 dB from 7% and 29 dB, respectively when driven with the 400 MHz test signal. Further reduction of the distortion was achieved by applying DPD of case (d), however, the EVM and ACPR were limited to 2.5-1.3% and 38-47 dB. The best signal metrics, i.e. EVM (1.7-0.6%) and ACPR (45-51 dB) were obtained by applying the proposed DPD of case (e). Fig. 2.11 shows the output spectrum with all five cases when the tripler is driven with 400 MHz test signal.

It is to be noted that an attempt was made to improve the linearizability of DPD case (d) when the tripler is driven with 400 MHz by increasing the number of coefficients from 33 to 158. However, only limited linearization results was achieved compared to the proposed DPD of case (e) with 57 coefficients.

Table 2.8: Linearization results for a frequency tripler centered at 63 GHz

			Only static		With memory	
		(a)	(b)	(c)	(d)	(e)
BW: 100 MHz	Settings	-	(3,5,0,0)	(9,0,-)	(3,5,2,2)	(9,4,5)
	S	-	1	1	1	2
	# Coeff	-	8	4	33	57
	ACPR L/U (dB)	31 / 31	37 / 38	37 / 38	43 / 42	51 / 51
	EVM (%)	6	2.3	2.3	1.3	0.6
BW: 200 MHz	Settings	-	(3,5,0,0)	(9,0,-)	(3,5,2,2)	(9,6,5)
	S	-	1	1	1	3
	# Coeff	-	8	4	33	57
	ACPR L/U (dB)	29 / 30	43 / 43	43 / 43	47 / 46	49 / 49
	EVM (%)	8.4	1.5	1.5	1.3	1.2
BW: 400 MHz	Settings	-	(3,5,0,0)	(9,0,-)	(3,10,2,2)	(9,4,5)
	S	-	1	1	1	2
	# Coeff	-	8	4	158	57
	ACPR L/U (dB)	30 / 29	33 / 33	33 / 33	38 / 39	45 / 45
	EVM (%)	7	4.4	4.3	2.5	1.7
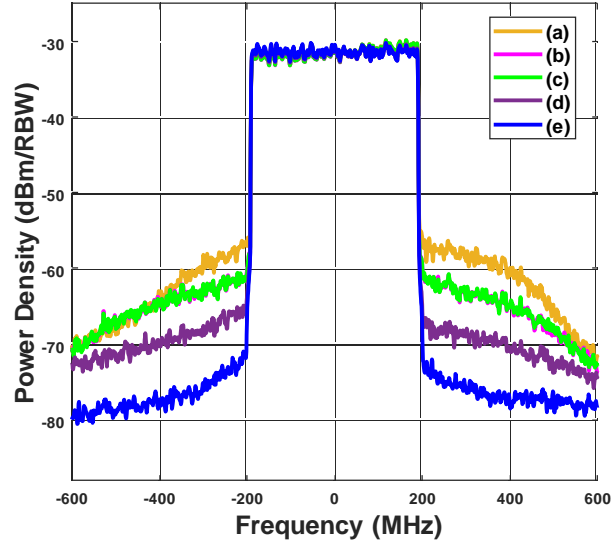
Figure 2.11: Measured output spectra of frequency tripler driven with OFDM signal of modulation BW 400 MHz: (a)After only cube root applied; (b) After memoryless DPD of [1] applied; (c) After memoryless proposed DPD applied; (d) After DPD of [1] applied; (e) After proposed DPD applied.

2.3.4 Linearization of Frequency Quadrupler

Table 2.9 and Fig. 2.12 summarize the linearization results of the frequency quadrupler. Based on these results, the quadrupler behaviour deviated significantly from the ideal quartic envelope transformation as significant residual distortions were observed when fourthroot DPD was applied (case (a)). As previously observed with the doublers and tripler, while the DPDs of cases (b)-(e) helped with mitigating some of the residual distortion, the proposed DPD of case (e) shows the best performance especially for the test signal with 400 MHz BW (see Fig. 2.12) where it is the only case where the EVM was lowered to 1.6% and the ACPR attained 45 dB. It is to be noted that the construction of the quadrupler using of-the-shelf two doublers used in the previous experiments engendered an irregular frequency response and non-negligible inter-stage mismatch and complicated further the linearization of the cascade. This explains the need for higher number of coefficients to achieve good signal quality.

39

Table 2.9: Linearization results for a frequency quadrupler centered at 25 GHz

|			Only static		With memory	
		(a)	(b)	(c)	(d)	(e)
BW: 100 MHz	Settings	-	(3,5,0,0)	(10,0,-)	(3,5,3,3)	(10,9,4)
	S	-	1	1	1	3
	# Coeff	-	8	4	37	38
	ACPR L/U (dB)	30 / 30	48 / 43	48 / 43	46 / 47	53 / 53
	EVM (%)	7.3	1.5	1.4	1.4	0.9
BW: 200 MHz	Settings	-	(3,5,0,0)	(10,0,-)	(3,6,3,5)	(10,12,6)
	S	-	1	1	1	6
	# Coeff	-	8	4	61	80
	ACPR L/U (dB)	30 / 29	45 / 39	45 / 39	44 / 40	49 / 49
	EVM (%)	8.5	3.1	3.1	2.7	1.2
BW: 400 MHz	Settings	-	(3,5,0,0)	(10,0, -)	(3,5,4,4)	(10,24,4)
	S	-	1	1	1	6
	# Coeff	-	8	4	38	73
	ACPR L/U (dB)	30 / 28	39 / 35	39 / 35	41 / 36	46 / 45
	EVM (%)	9.1	5.7	5.7	4.5	1.6
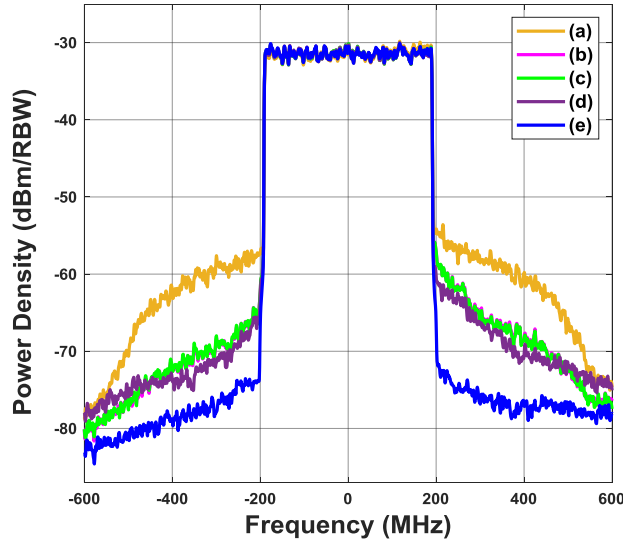
Figure 2.12: Measured output spectra of frequency quadrupler driven with OFDM signal of modulation BW 400 MHz: (a)After only fourth root applied; (b) After memoryless DPD of [1] applied; (c) After memoryless proposed DPD applied; (d) After DPD of [1] applied; (e) After proposed DPD applied.

2.4 Conclusions

This chapter proposed a novel DPD approach to linearize frequency multipliers when driven with wideband vector modulated signals. Experiments conducted using two distinct frequency doublers, a frequency quadrupler and a frequency tripler operating respectively around 25 GHz, 28 GHz and 63 GHz demonstrated excellent linearization capacity with acceptable number of DPD coefficients. The proposed DPD approach outperformed previous once especially when the modulation BW reached 400 MHz where an ACPR and EVM in the range of 45-49 dB and 1.8-1.3% were achieved at the output of the various frequency multipliers and under various test signals. It is important to note that the promising results obtained at the low-end of the mm-wave frequency range (25-63 GHz) pave the road for the application of the frequency multipliers based TX architecture for the generation of wideband vector modulated signals at higher mm-wave frequencies and potentially even to sub-THz frequencies.

Chapter 3

Single-Input-Single-Output Digital Predistortion for Frequency Multiplier based Beamforming Architecture

It has been discussed in previous chapters that shift to mm-wave and sub-THz frequency ranges is one of the solution to the demand of high data rate. However, as discussed earlier, there are several challenges at high frequency wireless signal generation and transmission, one of them being the TX output power. In an ideal free space propagation, Friis' equation for the received power (P_{RX}) can be expressed as transmitted power (P_{TX}), TX antenna gain (G_{TX}), RX antenna gain (G_{RX}) and the free space path loss (L_{FSP}) and given as,

$$P_{RX}(\text{dBm}) = G_{TX}(\text{dBi}) + P_{TX}(\text{dBm}) + G_{RX}(\text{dBi}) + L_{FSP}(\text{dB}), \quad (3.1)$$

where,

$$L_{FSP} = 10 \log_{10} \left(\frac{\lambda_c}{4\pi R}\right)^2, \quad (3.2)$$

λ_c is the wavelength which in a free space vacuum is related to frequency of operation, f_c as $\lambda_c = \frac{c}{f}$ and R is the distance between TX and RX. The Friis' equation in (3.1) and (3.2)
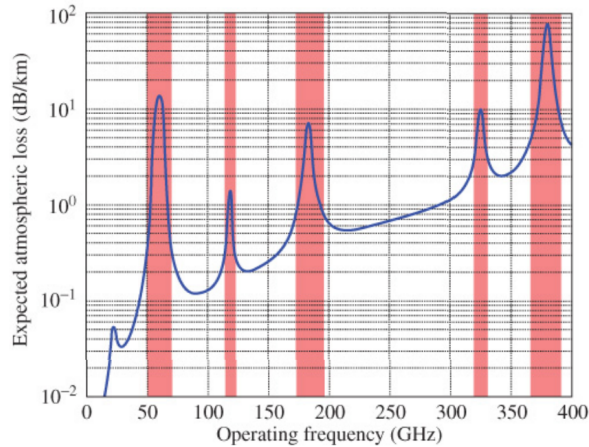
Figure 3.1: Atmospheric absorption at different frequencies [2]. The red highlighted portion represents region of high attenuation.

show that the free space path loss is inversely proportional to the square of $\frac{\lambda_c}{R}$ which simply means that with everything else being constant, the coverage area to keep the same P_{RX} decreases as the operating frequency increases. Additional to this problem, Fig. 3.1 shows that the atmospheric attenuation also increases with increasing operating frequency. As an effect, the coverage area gets more critically restricted. Hence, extracting high power at high frequency is even more challenging than it seems.

3.1 The Phased Array

Phased arrays have been studied as spatial antenna combiner with each element getting regulated phase in order to direct the power combined beam at various angles and increase the ouput radiated power. They are a solution to mitigate the challenge of coverage area at high frequency ranges by increasing the effective isotropic radiated power (EIRP) at the TX. EIRP is given as,

$$\text{EIRP} = \text{G}_{\text{TX}}(\text{dBi}) + \text{P}_{\text{TX}}(\text{dBm}). \tag{3.3}$$
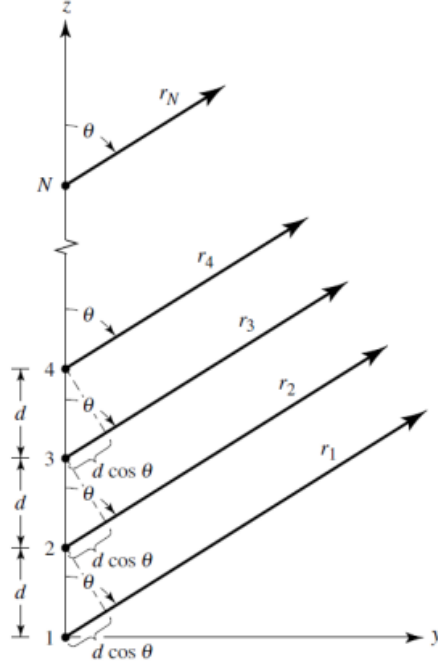
Figure 3.2: N Element Linear Phased Array [3].

Therefore, (3.1) becomes,

$$P_{RX}(dBm) = EIRP(dBi) + G_{RX}(dBi) + L_{FSP}(dB), \tag{3.4}$$

where L_{FSP} is the free space path loss. Consequently, G_{TX} or P_{TX} has to be increased in order to increase EIRP. G_{TX} can be increased by using larger antennas and phased array is a technique to increase antenna size by coherently combining numerous antenna elements. Fig. 3.2 shows an N element linear array where elements are spaced by distance d and nth antenna element direction of propagation is denoted as r_n at an angle θ. At far-field distance (i.e. $R > \frac{2D^2}{\lambda_c}$, where largest antenna dimension is denoted by D). Now, assume each antenna element gets a continuous wave (CW) sinusoid excitation with coefficient γ_n. As a result, the far-field combined coefficient (also known as array factor (AF)) for an isotropic antenna and linear array for $\phi = kdcos\theta$ and wave number $k = \frac{2\pi}{\lambda_c}$ can be written

as,

$$\mathrm{AF} = \sum_{n=1}^{N} \gamma_n e^{-j(n-1)\phi}. \tag{3.5}$$

Here, if $\gamma_n = |\gamma_n| e^{-j(n-1)\phi}$ which means that successive coefficients are ϕ apart. In this case, the combined signal in far-field is greater than isotropic single antenna element due to in-phase combination of all elements. For instance, for special case of same magnitude of all the coefficients, the combined signal in far-field is $N\times$ greater than isotropic single antenna element, i.e., $\mathrm{AF} = N|\gamma_n|$. Now, in order to direct the beam at certain direction, one can give proper phase excitations to different antenna elements. The arrays employing such technique are called beamforming or beamsteering arrays.

3.2 Literature Review

3.2.1 High Frequency Phased Array Architecture

Numerous researchers have explored the idea of phased arrays at high frequency (mm-wave and tera-Hertz) ranges for the reason that they are an attractive solution to achieve both higher EIRP and beam steering possibility. Different techniques have been discussed in literature to increase RF output power using phased arrays. These include on-chip power combining using transformers [42,43], Wilkinson couplers [44–47], or free-space (also known as quasi-optical or spatial) combining [46–52] These power combining techniques motivate the generation of high power at high frequency ranges However, the transformer and Wilkinson-based approach only suffice for a few number of TX chains and show limited performance otherwise due to finite quality factor (Q) of the underlying passive components. In contrast to this, spatial power combining takes advantage of OTA (also known as LSMA architecture) combining therefore it is 100% efficient theoretically (with the assumption of calibrated phase and amplitude distribution among different sub-arrays and no antenna or other losses) and low cost solution. Spatial combining made its headway in 1980s with two different architectures: the grid and the antenna topology. Both design techniques make use of multiple TX chains and antennas. The grid approach uses antenna
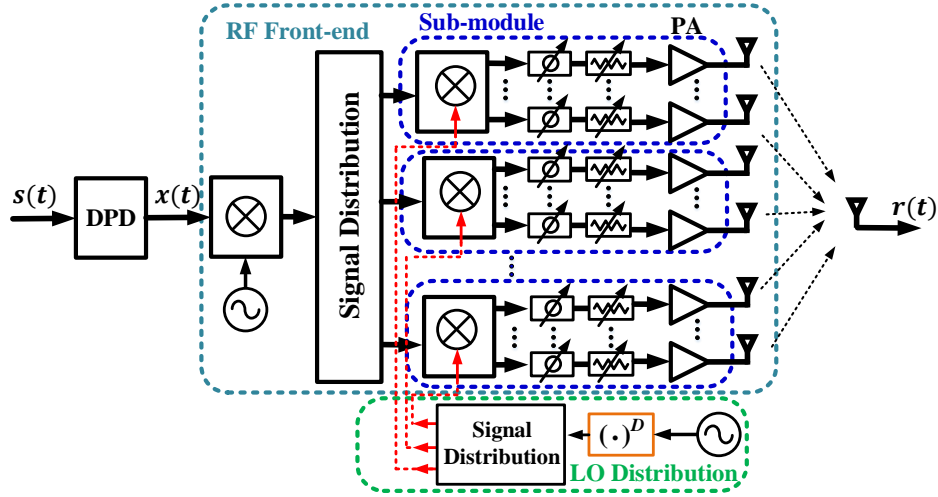
Figure 3.3: Conventional PA-based RF beamforming architecture with DPD.

element spacing of $0.1 - 0.2\lambda$ [49,52] while the later uses $0.5 - 1\lambda$ spacing between antenna elements. Each chain/antenna element is designed considering the mutual coupling among individual elements in antenna-based approach [49,53]. The authors in [50] showed a 256 element array at 44 GHz. Similarly, the authors in [51] demonstrated a grid amplifier with spatial combining around 30 GHz, while the authors in [52] presented a grid amplifier 64 element antenna array operating at 79 GHz. In addition to get higher output power using spatial combining, the authors in [52] implemented a two stage cascade unit cell to increase overall gain of single TX chain. Likewise, the authors in [46] demonstrated a 3×3 antenna array around 95 GHz. Moreover, in [47], the authors presented a 44 a transceiver phased array at operating frequency of 90-100 GHz. Moreover, these multiple chains and multiple antennas architecture can be characterized in three different beamforming arrangements, namely, RF/analog, digital or combination of both i.e., hybrid. RF beamforming applies phase and amplitude variations on analog signal while digital beamforming applies these variations on digital signal before the DAC. In practice, RF beamforming architecture is widely acquired by researchers at mm-wave frequency ranges due to the cost-efficient and less complicated setup [7,8] as compared to digital and hybrid beamforming architecture. Fig. 3.3 shows a generic RF beamforming TX architecture, where the RF front-end is divided into sub-modules and the input signal is located at an intermediate frequency

lower than the targeted operating frequency. This strategy is typically followed to reduce the parasitics and losses of the signal distribution network. In Fig. 3.3, the frequency up-conversion is performed at the sub-module level using high-frequency LO signals. Often, the LO signals are generated using a common frequency multiplier and a high-frequency LO distribution network (see Fig. 3.3) or by using multiple frequency multipliers located at each sub-module.

The RF beamforming architecture in Fig. 3.3 is fundamentally limited by the PA in terms of the maximum frequency of operation. In fact, for a given semiconductor technology, the maximum operating frequency of the PA is generally much lower than the maximum oscillation frequency. This motivated the authors in [54–58] to develop a frequency-multiplier-based RF beamforming architecture as a means to maximize the achievable operating frequency for a given fabrication technology. This architecture minimizes the impacts of the input signal and LO distribution networks as they operate at lower frequencies compared to Fig. 3.3. The researchers in [54] demonstrated free-space combining by utilizing frequency triplers based 14×14 array at 93 GHz. Furthermore, the authors in [57] presented an eight element phased array around 300-400 GHz. The design consists of amplifiers, phase shifters, frequency quadruplers and on-chip antennas. However, the work presented in [54–58] is only feasible for low order modulation signals and unable to handle complex modulated signals and the strong nonlinearity exhibited by typical frequency multipliers meant the experimental results presented in those works were limited to signals with constant envelopes.

3.2.2 SISO DPD for PA-Based RF Beamforming Architecture

In order to improve the linearity vs efficiency trade off, several attempts have been made to extent the SISO DPD application to linearize PA-based RF beamforming architectures. The extension of the DPD technique to an array can be grouped into two different technique, one using single input DPD which accounts for input as forward travelling waves only and other using dual input DPD that incorporates input waves as forward as well as reverse waves. Previous attempts to implement single input DPD approach is described in [59–62] while [63, 64] implemented dual input DPD scheme. The authors in [63] de-

vised a two input DPD scheme after studying antenna crosstalk and array behavior and demonstrated a four PA array TX, driven by digitally modulated 5 MHz signal at 2.1 GHz, and linearized the array using four different PD modules. On the other hand, the authors in [59] opted for a trade off between power consumption and linearization capability and demonstrated single input DPD model to linearize each sub-array separately. Furthermore, the work of [61] focused on using single PD module to linearize whole array and showed promising simulation results using polynomial based PD model. Single input DPD model seems an attractive solution for RF beamforming architecture where input to each individual PA is not possible and as a result, one PD module has to be used to linearize whole array. However, the authors in [59, 61] did not account for memory effects of PA, as well as, antenna mismatch and crosstalk.

Furthermore, the authors in [60] showed linearization of 2×2 array, driven with 10 MHz modulated signal and operating at 2 GHz, using single input and single PA feedback DPD model. The authors in [60] claim that since PA nonlinearity depends upon input amplitude and not phase therefore in RF beamforming one can use one PA output and use as feedback signal to linearize whole array.

Afterwards, the authors in [62] proposed a single user stream based SISO DPD model and linearized 64 element array operating at 28 GHz and driven by 320 MHz digitally signal. The work in [62] interestingly incorporated the antenna mismatch and crosstalk in the DPD coefficients. Furthermore, authors of [62] extended the work to [64] and incorporated a dual input SISO DPD to account for the steering angle depended antenna array load modulation. All in all, none of the attempts have been made to linearize a frequency-multipliers-based beamforming architecture.

3.3   Novelty of this work

In this work, a frequency-multipliers-based RF beamforming architecture is proposed which incorporates a SISO DPD module (see Fig. 3.4) to transmit vector-modulated signals with high PAPR. A proof-of-concept validation was conducted using first a connectorized measurement test with 2 and 4 TX chain power combining, followed by a 2×2 RF beamforming
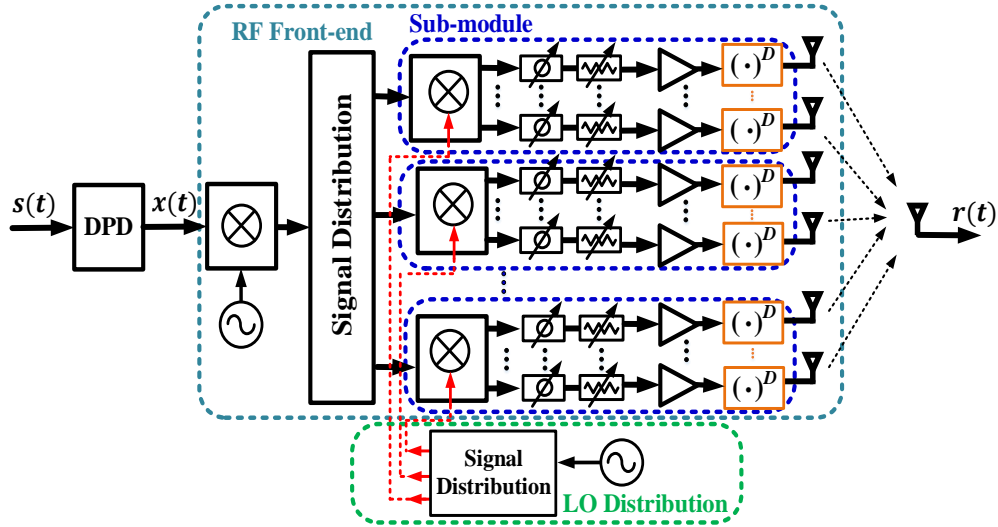
Figure 3.4: Proposed frequency-multiplier-based RF beamforming architecture with DPD, where $(.)^D$ represents a frequency multiplier with multiplication factor D.

array that included four frequency-doublers, all operating at 28 GHz.

3.4 SISO Model For Frequency-Multiplier-Based RF Beamforming Arrays

As previously mentioned, the transmission of signals with high PAPR using a frequency-multiplier-based beamforming architecture is hindered by the frequency multiplier's non-linearity. Recent work and a proposed DPD scheme is discussed in Chapter 2 of this thesis that successfully mitigated the nonlinearity exhibited by a frequency-doubler-based single-branch high-frequency source.. Motivated by the success of SISO DPD to linearize PA-based RF beamforming architectures [59–64], this work extends the frequency-multiplier-based RF beamforming architecture of [55–58] by adding SISO DPD to mitigate the non-linearities exhibited by the constituent frequency multipliers when transmitting signals with a high PAPR, see Fig. 3.4.

To derive a SISO DPD function suitable for linearizing the nonlinear behavior of the RF
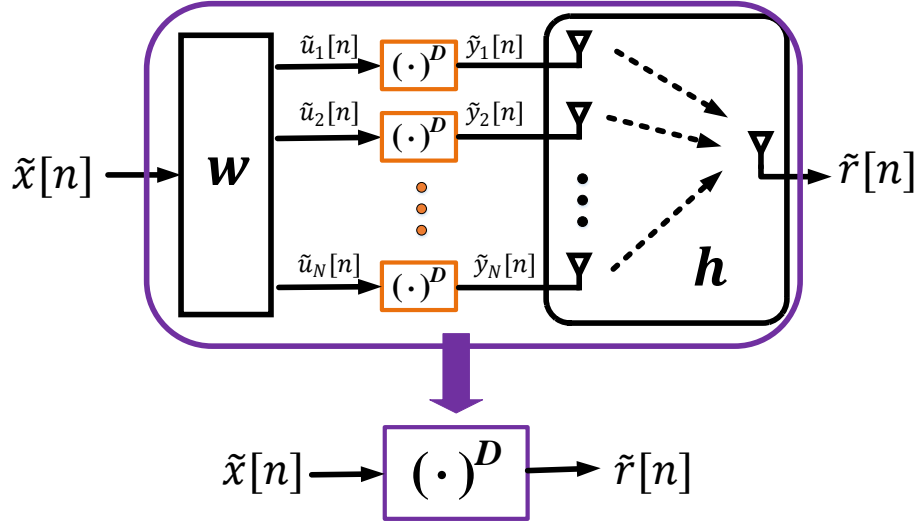
Figure 3.5: Behavioral model of frequency-multiplier-based RF beamforming array using an equivalent SISO describing function.

front-end in Fig. 3.4, the constituent components were replaced with their corresponding baseband equivalent models as shown in Fig. 3.5. Here, $(.)^D$, $\boldsymbol{w}$, and $\boldsymbol{h}$ represent a frequency multiplier with multiplication factor D, the beamforming weight vector, and the channel response vector in the far-field, respectively. Furthermore, N denotes the number of frequency multipliers/antenna elements.

Let $\tilde{x}[n]$ be the CBBE input signal of the RF front-end of a frequency-multiplier-based RF beamformer. Hence, the CBBE input signal to each frequency multiplier can be expressed as $\tilde{u}_i[n] = \tilde{x}[n] \times w_i$, where $w_i = e^{j\phi_i/D}$ and ϕ_i is the i'th antenna beamforming coefficient. Moreover, the CBBE output signal of the i'th frequency multiplier, $\tilde{y}_i[n]$, can be modelled using a SISO baseband nonlinear describing function, $f(\tilde{u}_i[n], \tilde{u}_i[n-1], \ldots, \tilde{u}_i[n-M]; \boldsymbol{\alpha}^{(i)})$ where M denotes the memory depth and $\boldsymbol{\alpha}^{(i)}$ is a vector comprising the corresponding coefficients of f. For the purpose of illustration and to simplify the derivations, a memoryless forward model is used to represent the nonlinearity of a frequency multiplier. Therefore, $\tilde{y}_i[n]$ can be written as,

50

$$\tilde{y}_i[n] = \sum_{k=0}^{K} \alpha_k^{(i)} \tilde{u}^D[n]|\tilde{u}[n]|^{2k}$$

$$= \sum_{k=0}^{K} \alpha_k^{(i)} e^{j\phi_i} \tilde{x}^D[n]|\tilde{x}[n]|^{2k}, \qquad (3.6)$$

where K is the maximum nonlinearity order. Assuming a coherent combining of the frequency multipliers' output signals in the far-field, the CBBE received signal, $\tilde{r}[n]$, is given as,

$$\tilde{r}[n] = \sum_{i=0}^{N-1} h_i \tilde{y}_i[n], \qquad (3.7)$$

Substituting (3.6) into (3.7), we get,

$$\tilde{r}[n] = \sum_{i=0}^{N-1} \sum_{k=0}^{K} h_i \alpha_k^{(i)} e^{j\phi_i} \tilde{x}^D[n]|\tilde{x}[n]|^{2k}$$

$$= \sum_{k=0}^{K} \sum_{i=0}^{N-1} h_i \alpha_k^{(i)} e^{j\phi_i} \tilde{x}^D[n]|\tilde{x}[n]|^{2k}. \qquad (3.8)$$

Under the line-of-sight assumption and in the direction of the main beam, $h_i = e^{-j\phi_i}$. Hence,

$$\tilde{r}[n] = \sum_{k=0}^{K} \sum_{i=0}^{N-1} \alpha_k^{(i)} \tilde{x}^D[n]|\tilde{x}[n]|^{2k}$$

$$= \sum_{k=0}^{K} \beta_k \tilde{x}^D[n]|\tilde{x}[n]|^{2k}, \qquad (3.9)$$

where $\beta_k = \sum_{i=0}^{N} \alpha_k^{(i)}$, are the model coefficients of the aggregate nonlinearities exhibited by the different frequency multipliers. Based on (3.9), the relationship between the CBBE input signal to the RF front-end and the CBBE received signal in the far-field can be represented by a SISO describing function. Consequently, SISO DPD can be used to linearize the distortions exhibited by the array of frequency multipliers and to ensure a good quality signal in the far-field. In this work, the SISO DPD model proposed in [1], used to linearize a single frequency multiplier, will be amended to linearize frequency-multiplier-based RF beamforming arrays. It is of note that the above derivation can be applied to frequency multipliers exhibiting memory effects without the loss of generality.

3.5   Test and Measurement Results

As a proof of concept, in this section, we first perform a frequency doubler based coherent power combining TX architecture using Wilkinson power combiner followed by OTA four element (2×2) RF beamforing test. Note that the connectorized test was first investigated before the OTA test because the former is less sensitive to channel calibration and isolation and it is interesting to validate the proposed idea with ideal condition of higher isolation between the chains and no channel response. Also, it is worth mentioning that in all following measurement tests, the frequency response of TX and RX in each chain is compensated for. The relative calibration among several chain has also been performed

3.5.1   Connectorized Test Using 2 TX Chains

Test and Measurement Setup

The test setup shown in Fig. 3.6 is utilized to demonstrate the coherent power combining using Wilkinson power combiner with two TX chains and two frequency doublers. The setup uses an AWG (M8190A from Keysight Technologies) to generate the signals at IF of 1.75 GHz, followed by a balun (BALH0010 from Marki Microwave) to improve the signal dynamic range and LPF (11SZ10-4000/T8000-O/O from K&L) to reject other Nyquist regions. A custom built IF board containing a hybrid 90° coupler is then used to convert the IF signal into inphase and quadrature signal components so that an IQ mixer can be used later to upconvert the test signal and reject the image. The IF board also contains a bias-T to cancel the LO feed-through and an onboard driver amplifier. The IF board is followed by a cascade of an IQ mixer (MLIQ-0416L from Marki Microwave) to upconvert the IF test signal to 14 GHz and a custom built LPF with cut off frequency at 16 GHz. Afterwards, the generated OFDM modulated test signal, located around 14 GHz, by the mixer-based frequency up-converter undergoes filtering and power amplification stages. The signal is amplified using a gain amplifier (MAAM-011109 from MACOM) and finally being fed to the frequency doublers (HMC-578 from Analog Devices) after Wilkinson power divider (PD-0140 from Marki Microwave). The outputs of the frequency doublers are then used to feed Wilkinson power combiner centered at 28 GHz. Afterwards, a downconversion

mixer (MM1-1140H from Marki Microwave) is used to convert the RF signal to IF in order to capture the signal using 8 GHz analog BW, 20 GS/s, 10-bit oscilloscope (MSOS804A from Keysight Technologies). Note that the sample of the signal is extracted through a directional coupler (110040010K from Krytar, not shown in Fig 3.6) to train the PD blocks.

The signals and DPD scheme used for validation are the same as given in Chapter 2, i.e., OFDM test signals with modulation BWs equal to 100 MHz, 200 MHz and 400 MHz with 64-QAM, 256-QAM and 256-QAM symbols, respectively. The measurement metrics, i.e., EVM and ACPR, are also kept same as Chapter 2. Moreover, in case of multiple chains and power combining, it is important to investigate the linearization results without RX and channel calibration applied. It would be very interesting if the linearization results are within the standard specifications without applying any RX calibration. This would be very less troublesome because otherwise the channel from each antenna element to the probing antenna as well as RX frequency response has to be compensated for. The known reference source (comb generator U9391G from Keysight Technologies) used for RX calibration exhibits very less power in case of OTA measurements hence some amplification has to be done which makes the RX calibration a bit complicated.

DPD Measurement Results

Table 3.1 presents the summary of the measurement results for 100 MHz, 200 MHz and 400 MHz instantaneous BW signals for two element power combined using Wilkinson power combiner where (a) refers to the case where only square root is applied, (b) refers to the case with the proposed DPD applied without RX calibration and (c) refers to the case with the proposed DPD applied with RX calibration. It can be concluded from the results that applying only square root is insufficient to remove out of band regrowth. Therefore, the proposed DPD scheme was applied and excellent linearization results were achieved with ACPR improvement of 31 dB in 100 MHz signal, 27 dB in 200 MHz signal and 24 dB in 400 MHz signal while EVM was improved from ∼12% to ∼0.7 % in all signal BW cases. Additionally, it is shown that acceptable results can be achieved without using RX calibration while they deteriorate as BW increases from 100 MHz to 400 MHz.

Fig. 3.7 shows at left hand side, ACPR and EVM variation as the parameter $\mathcal{S}$ changes
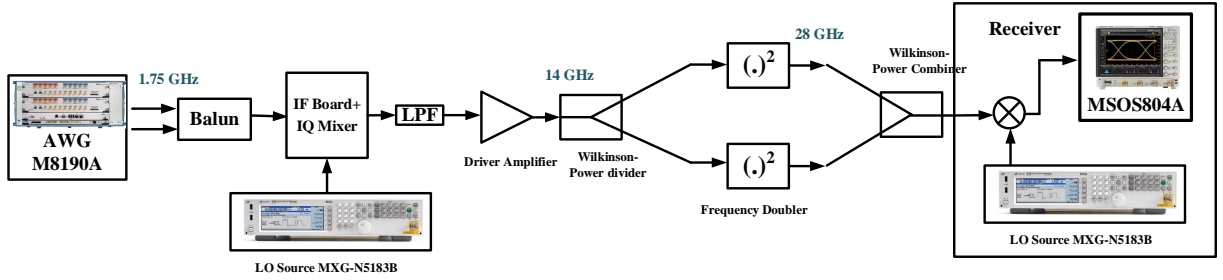
Figure 3.6: mm-wave test and measurement setup to validate connectorized and coherent power combining using two elements.

from 1 to 5, keeping the number of DPD coefficients constant at 44. The curve shows the best $\mathcal{S}$ for 100 MHz signal is 3 or 4, therefore we chose $\mathcal{S} = 3$. At the right hand side, the 100 MHz output spectra for case (a)-(c) with two-element TX chain is shown for $\mathcal{S} = 3$.

Similarly, Fig. 3.8 and show ACPR and EVM vs $\mathcal{S}$ results and output spectra for 200 MHz and 400 MHz signal. The left hand side curve shows $\mathcal{S} = 3$ for 200 MHz and $\mathcal{S} = 4$ for 400 MHz.

The measurement results provided above show potential of linearizing the combined signal using a SISO DPD with only one feedback path, i.e., one transmitter observation receiver (TOR). Ultimately, it is interesting to observe the individual chain's output spectrum before combining. In order to perform this test, the Wilkinson power combiner was removed after the linearization of combined signal and the output spectrum at each chain was recorded. Table 3.2 shows the summary of this measurement test. It can be clearly observed that the individual chains were not linearized completely while linearizing the combined signal, giving ACPR of 50-53 dB. On the other hand, the combined chains were linearized upto ACPR of 57 dB giving 31 dB ACPR and 11 % EVM improvement as compared to only square root applied. Fig. 3.10 shows the output spectra of the discussed cases.

Table 3.1: Linearization results of 2-TX chain power combined using Wilkinson power combiner

	Signal BW: 100 MHz			Signal BW: 200 MHz			Signal BW: 400 MHz		
	(a)	(b)	(c)	(a)	(b)	(c)	(a)	(b)	(c)
Settings	-	(20,6,4)	(20,6,4)	-	(20,12,4)	(20,12,4)	-	(20,16,4)	(20,16,4)
S	-	3	3	-	6	6	-	4	4
# Coeff	-	44	44	-	44	44	-	178	178
ACPR (L/U) (dB)	26 / 26	57/56	57/ 57	26 / 26	50/50	53/53	26 / 26	46/48	50/ 50
NMSE (%)	14	1.0	0.9	13.6	1.4	1.0	12.8	2.2	1.5
EVM (%)	11.8	0.7	0.7	12.7	0.8	0.7	12	1.1	0.8

Table 3.2: Linearization results of each chain vs 2-TX chain power combined using Wilkinson power combiner

	Signal BW: 100 MHz			
	$\sqrt{(.)}$ (Combined)	$\sqrt{(.)}$ + DPD (Combined)	$\sqrt{(.)}$ + DPD (Ch1)	$\sqrt{(.)}$ + DPD (Ch2)
Settings	-	(20,10,4)	(20,10,4)	(20,10,4)
S	-	5	5	5
# Coeff	-	44	44	44
ACPR (L/U) (dB)	26/26	57 / 57	50 / 50	52 / 53
NMSE (%)	14	0.9	2.4	1.7
EVM (%)	11.8	0.7	0.94	0.82

Figure 3.7: Left: Measured ACPR and EVM results with modulation BW 100 MHz versus different S values. Here, ACPR indicates the average ACPR value of lower and upper ACPR values. Right: Measured output spectra of 2-TX chains combined with Wilkinson power combiner, driven with OFDM signal of modulation BW 100MHz: (a) After only square root applied; (b) After proposed DPD (without RX calibration) applied; (c) After proposed DPD (with RX calibration) applied.

3.5.2 OTA Test Using 2 Elements (1×2 Antenna Array)

Once the connectorized tests were performed, the next step is to validate the idea with OTA measurements. First the tests are conducted to prove the ability of the SISO DPD to linearize a frequency-doubler-based 1×2 beamforming front-end that includes linearly polarized antenna elements.

Test and Measurement Setup

The setup uses same components as described in Section 3.5.1 with 1×2 printed circuit board patch antenna array replacing the Wilkinson combiner as shown in Fig. 3.11. For DPD training purposes, the received signal is captured using a probing horn antenna positioned in the far-field.
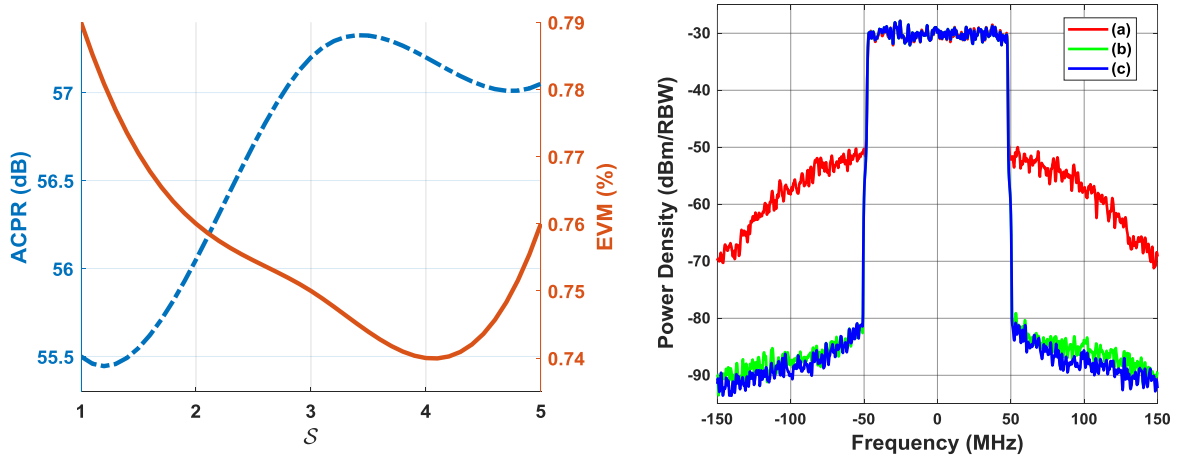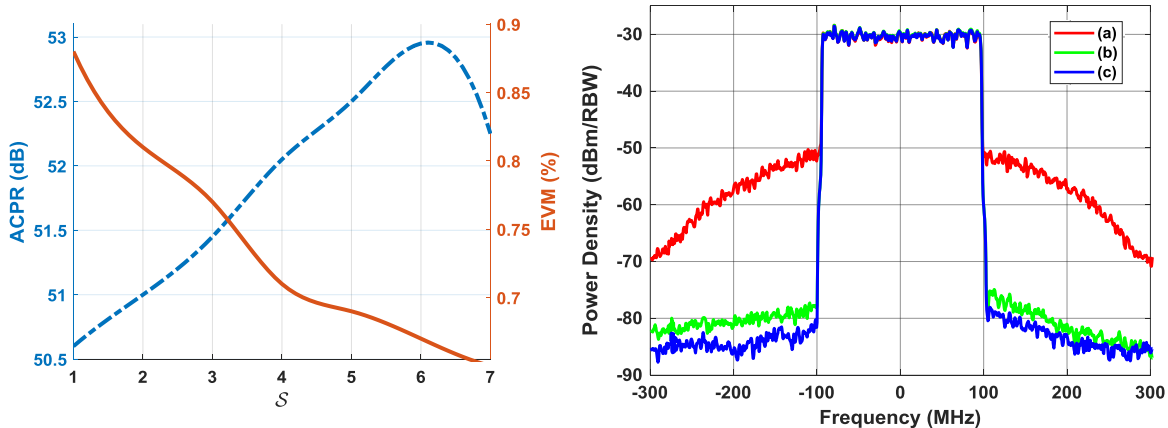
56

Figure 3.8: Left: Measured ACPR and EVM results with modulation BW 200 MHz versus different S values. Here, ACPR indicates the average ACPR value of lower and upper ACPR values. Right: Measured output spectra of 2-TX chains combined with Wilkinson power combiner, driven with OFDM signal of modulation BW 200MHz: (a) After only square root applied; (b) After proposed DPD (without RX calibration) applied; (c) After proposed DPD (with RX calibration) applied.

DPD Measurement Results

Table 3.3 shows the DPD measurement results when OFDM signals of 100 MHz, 200 MHz and 400 MHz modulation BW were applied, where (a) represents the case with only square root applied and (b) represents the case with the proposed DPD applied. In these tests, the DUT were pushed more into compression to extract more conversion gain, as discussed in Chapter 2, resulting as higher starting ACPR i.e., ~ 23 dB. Similar to the connectorized test described earlier, the SISO DPD showed excellent linearization results when applied to OTA measurement setup. The ACPR was improved from 23 to 54 dB, 21 to 50 dB and 24 to 46 dB and EVM was improved from 18.5% to 0.8%, 22% to 1.2% and 15.3% to 1.8% in 100, 200 and 400 MHz cases respectively. Note that these results were obtained with the RX and channel calibration applied. As we moved from connectorized to OTA measurements, we realized that channel calibration becomes critical. However, the results obtained without RX calibration are also within the third generation partnership project
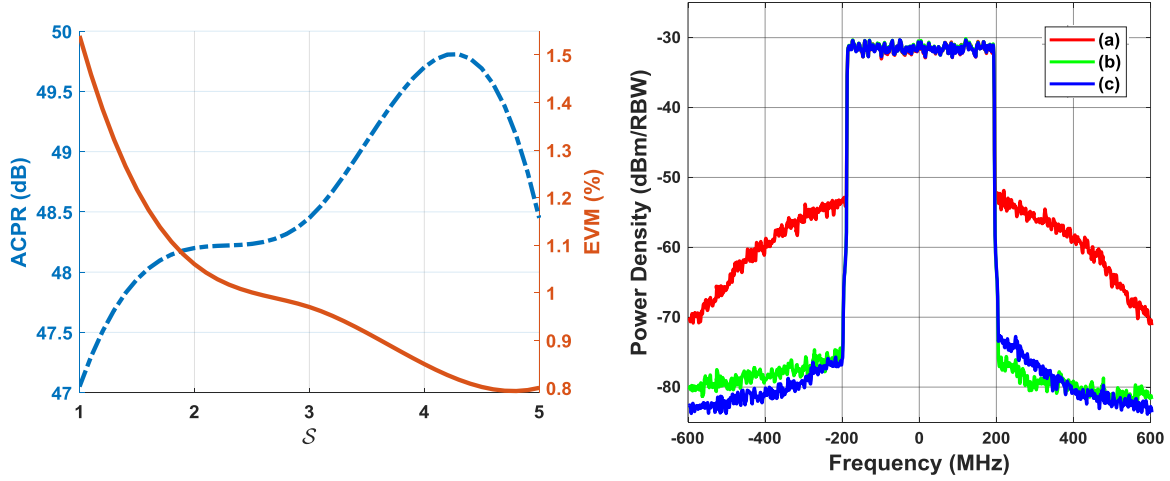
57

Figure 3.9: Left: Measured ACPR and EVM results with modulation BW 400 MHz versus different S values. Here, ACPR indicates the average ACPR value of lower and upper ACPR values. Right: Measured output spectra of 2-TX chains combined with Wilkinson power combiner, driven with OFDM signal of modulation BW 400MHz: (a) After only square root applied; (b) After proposed DPD (without RX calibration) applied; (c) After proposed DPD (with RX calibration) applied.

(3GPP) standard. Figs. 3.12, 3.13 and 3.14 show the curve to find out optimum S and the measured output spectra for all three modulation BWs. In order to demonstrate the results with and without RX calibration, Fig. 3.14 compares case (b) and (c) where (c) represents the case without RX calibration applied. The spectrum in case (c) has ACPR of 44dB and EVM 1.9% as compared to case (b) with ACPR 46 dB and EVM 1.8%.

3.5.3 OTA Test Using 4 Elements (2×2 Antenna Array)

The promising DPD linearization results obtained in the previous subsection with 2-antenna elements motivated to extend and validate the idea at broadside with 4-antenna elements and 4 frequency doublers, as shown in Fig. 3.15.

Fig. 3.16 shows the experimental setup devised to prove the ability of the SISO DPD
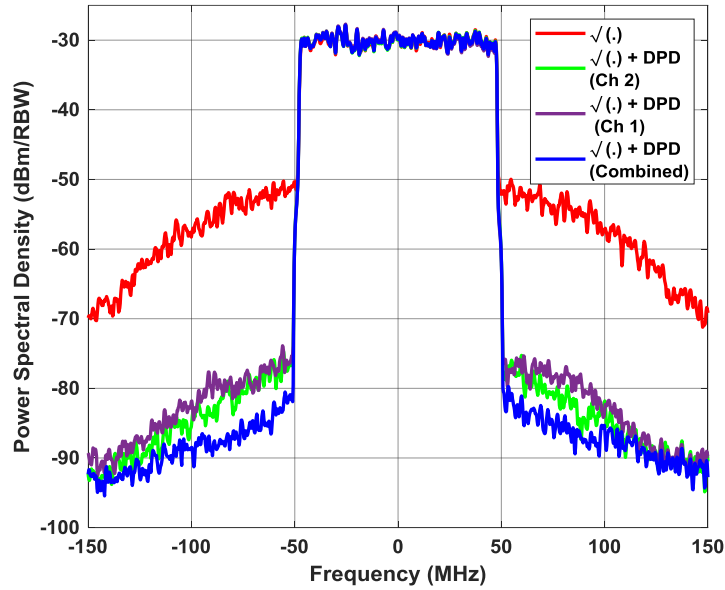
Figure 3.10: Measured output spectra of channel-1, channel-2 and combined 2-TX chains, driven with OFDM signal of modulation BW 100 MHz after proposed DPD applied.

Figure 3.11: mm-wave test and measurement setup to validate broadside OTA coherent power combining using two elements.

to linearize a frequency-doubler-based 2×2 beamforming front-end that includes linearly polarized antenna elements.

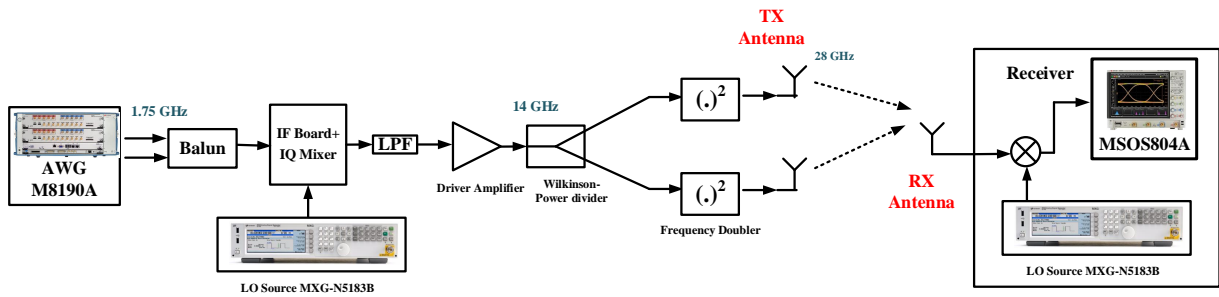The setup used is the same as described earlier. TX and RX calibrations were applied in
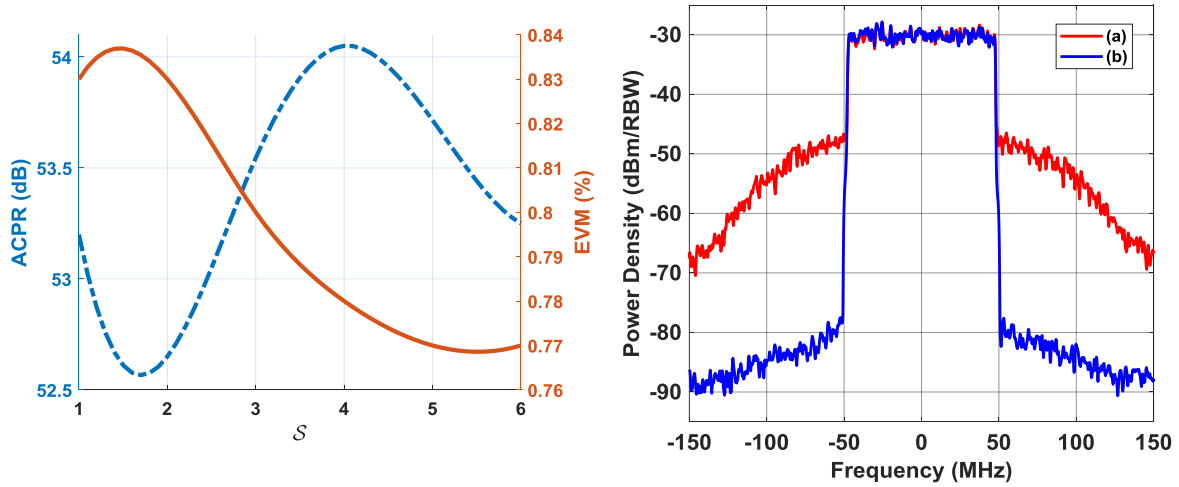
Figure 3.12: Measured output spectra of OTA broadside 2-TX chains, driven with OFDM signal of modulation BW 100 MHz: (a) After only square root applied; (b) After proposed DPD applied.

order to ensure an AF close to the theoretical value of $20 \times log_{10}(4) = 12$ dB. Experiments were conducted using two test signals with modulation BWs equal to 100 MHz and 400 MHz with 64-QAM and 256-QAM symbols, respectively.

Fig. 3.17 and Fig. 3.18 show the output spectra (green colored plots) of the received signals in the far-field for both 100 MHz and 400 MHz test signals, respectively, after application of the square-root function of the test signals. These spectra highlight the significant out-of-band emissions attributable to the deviation of the frequency doublers from the ideal $(.)^2$. It can be seen in the figures that pre-processing the test signals using the DPD function trained using a nonlinearized far-field received signal allowed for excellent compensation of the out-of-band emissions (see blue colored plots) for both test signals. Table 3.4 includes the ACPR and EVM of the far-field received signals, obtained when the test signals are pre-processed using either i) only the square-root function or ii) the cascade of the square-root function plus the trained SISO DPD. In the case of a test signal with 100 MHz modulation BW, application of the SISO DPD allowed for an improvement of the ACPR and EVM from 30 dB and 7.9% to 52 dB and 0.9%, respectively. Similar

Table 3.3: Linearization results of 2-TX chain OTA power combined

	Signal BW: 100 MHz		Signal BW: 200 MHz		Signal BW: 400 MHz	
	(a)	(b)	(a)	(b)	(a)	(b)
Settings	-	(20,8,4)	-	(20,6,4)	-	(20,6,4)
S	-	4	-	3	-	3
# Coeff	-	44	-	44	-	44
ACPR (L/U) (dB)	23 / 23	54/54	21 / 22	50/50	24 / 24	46/47
NMSE (%)	21.4	1.2	23	1.85	18.3	2.2
EVM (%)	18.5	0.78	21.9	1.16	15.3	1.8

Figure 3.13: Left: Measured ACPR and EVM results with modulation BW 200 MHz versus different S values. Here, ACPR indicates the average ACPR value of lower and upper ACPR values. Right: Measured output spectra of OTA broadside 2-TX chains, driven with OFDM signal of modulation BW 200 MHz: (a) After only square root applied; (b) After proposed DPD applied.

improvements were observed for the test signal of 400 MHz BW. It is of note that during these experiments the DPD parameters were set to $N' = 10, M = 10, P' = 4$, and $S = 5$,
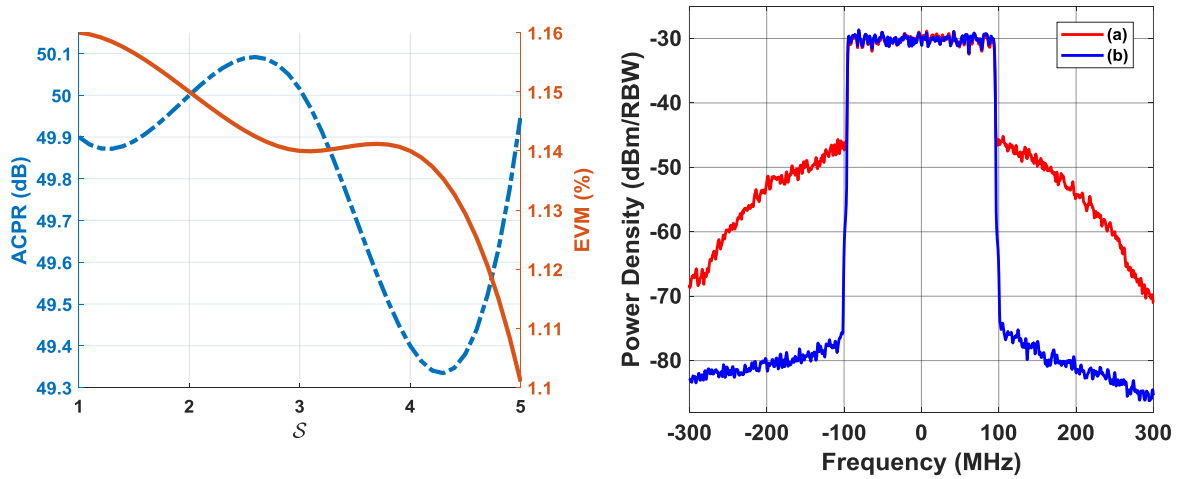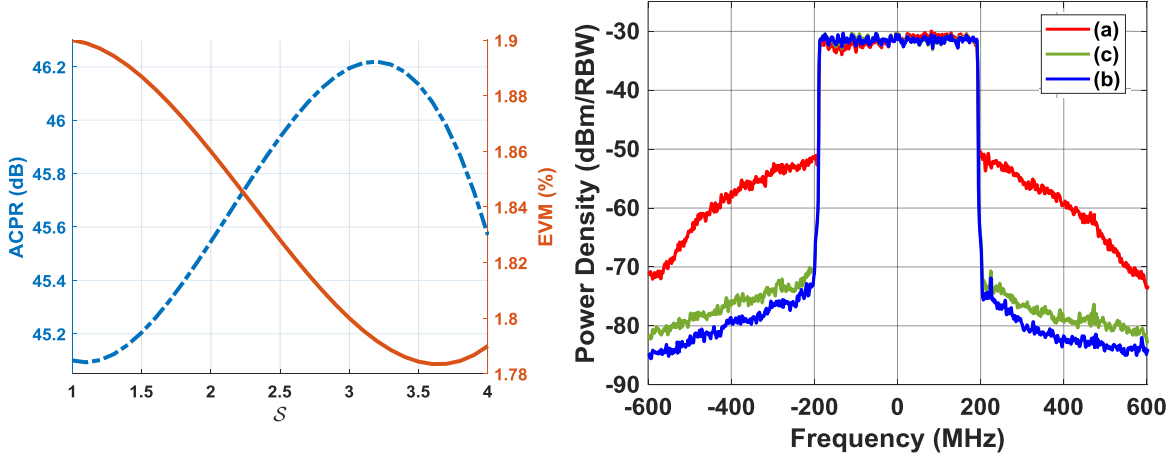
Figure 3.14: Left: Measured ACPR and EVM results with modulation BW 400 MHz versus different S values. Here, ACPR indicates the average ACPR value of lower and upper ACPR values. Right: Measured output spectra of OTA broadside 2-TX chains, driven with OFDM signal of modulation BW 400 MHz: (a) After only square root applied; (c) After proposed DPD (without RX+channel calibration) applied; (b) After proposed DPD (with RX+channel calibration) applied.
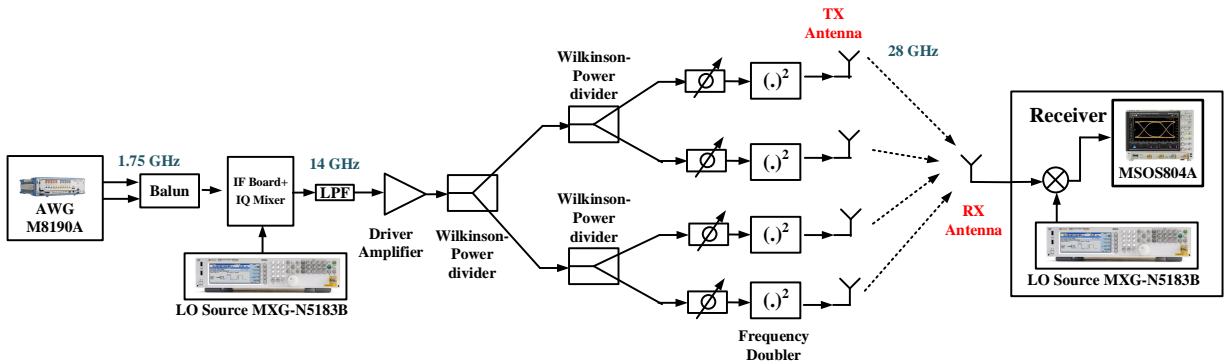
Figure 3.15: mm-wave test and measurement setup to validate broadside OTA coherent power combining using four elements.
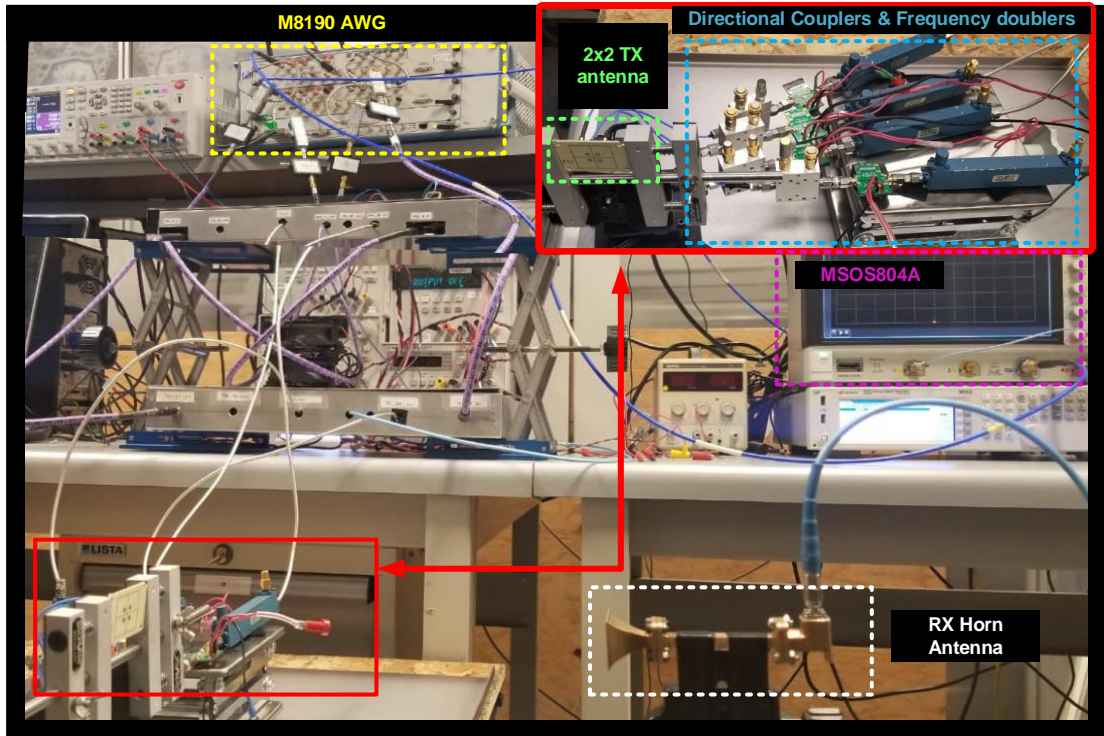
Figure 3.16: Experimental measurement setup.

totalling 39 coefficients.

Interestingly, based on Fig. 3.17 and Fig. 3.18, the spectra of the individual frequency-doubler output signals reveals residual out-of-band emissions higher than those measured in the far-field. This observation is further supported by the fact that the worst EVM was measured at the frequency-doubler's output, as opposed to in the far-field (see Table 3.4). This corroborates the theoretical prediction of the cancellation of the un-correlated distortions in the far-field. It also confirms the theory that linearizing the signal in the far-field does not require the same extent of linearization as the individual paths.

Figure 3.17: Measured output spectra of frequency-doubler array in the far-field driven with 100 MHz OFDM signal and with SISO DPD applied.

3.6 Conclusion

This chapter proposed a frequency-multiplier-based RF beamforming architecture. A theoretical formulation of the SISO DPD model was derived to linearize the proposed array when driven with vector modulated wideband signals. Experiments were conducted using a Wilkinson power combiner, 1×2 and 2×2 frequency-doubler-based RF beamforming array centered at an output frequency of 28 GHz. Connectorized and OTA measurement results showed that the proposed SISO DPD function successfully linearized the frequency-doubler-based array, giving excellent ACPR and EVM values for 100 MHz, 200 MHz and 400 MHz OFDM signals with PAPR of 11 dB, respectively. It is to note that, as a proof of concept, the measurement results were validated at 28 GHz; however, the proposed architecture can be extended to higher frequencies.

Table 3.4: ACPR and EVM measurement results.

		$\sqrt{(.)}$	$\sqrt{(.)}$ + DPD				
		Far-field	Far-field	Ch1	Ch2	Ch3	Ch4
BW: 100 MHz	ACPR L/U (dB)	30 / 29	53 / 52	48 / 48	45 / 44	44 / 45	49 / 48
	EVM (%)	7.9	0.9	1.3	1.3	1.3	1.1
BW: 400 MHz	ACPR L/U (dB)	35 / 33	47 / 47	40 / 39	38 / 40	39 /37	40 / 41
	EVM (%)	8.6	2.5	4.2	2.6	3.4	3.2

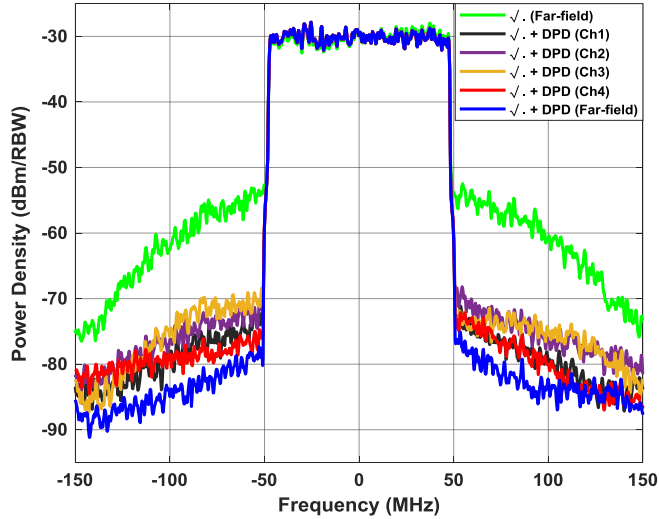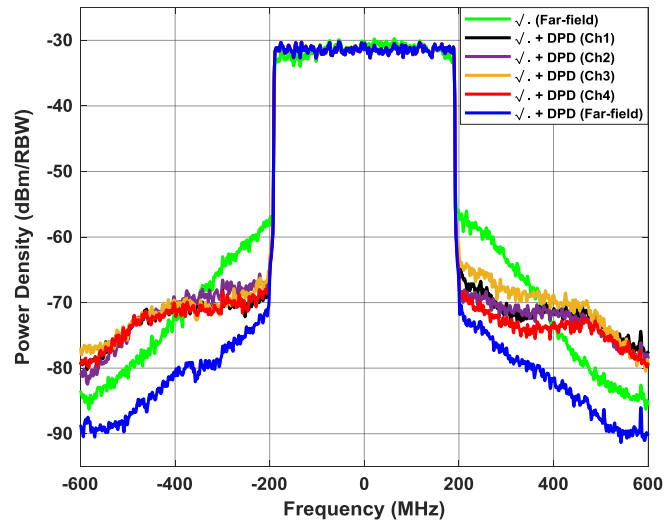Figure 3.18: Measured output spectra of frequency-doubler array in the far-field driven with 400 MHz OFDM signal and with SISO DPD applied.

Chapter 4

Conclusions

In this thesis, a novel DPD scheme to mitigate the non-idealities of the frequency multiplier-based high frequency vector signal source is presented. A frequency-multiplier-based RF beamforming architecture is then proposed to solve the challenge of low output power at high frequency ranges. In addition, a SISO DPD scheme to mitigate the impairments of frequency-multiplier-based array is also proposed.

In Chapter 2, different high frequency vector signal generators with their literature were first compared. Afterwards, a passband frequency model for frequency multipliers were discussed, followed by proposed augmented D^{th} order Volterra series construction. A detailed derivation on CBBE model of the augmented discrete-time Volterra series of order D is then presented. A DPD scheme for frequency multipliers is then devised. Afterwards, DPD training is discussed. Several experiments using frequency doublers, tripler and quadrupler to validate the proposed idea were performed and demonstrated using 100 MHz, 200 MHz and 400 MHz OFDM signals with 64-QAM, 256-QAM and 256-QAM symbols, respectively.

Chapter 3 began with the motivation of phased array architecture at high frequency ranges, followed by literature review on different beamforming architectures. Afterwards, a frequency-multiplier-based RF beamforming architecture was proposed to generate vector modulated signal with high radiation power. A SISO model was also presented to linearize the multiplier array. The measurement tests were provided to validate the proposed ar-

chitecture and SISO DPD scheme. Two different sets of measurement results were given using Wilkinson power combiner and printed circuit board based path antennas. All results showed excellent linearization capability.

4.1 Future Work

For the future of this work, the beamsteering ability and load modulation effects can be explored in the frequency-multiplier-based beamforming architecture. Furthermore, in case the frequency-multiplier-based TX architecture experiences the same load modulation effects as the PAs, then dual input DPD for frequency multipliers can be a very interesting research topic to investigate. Unlike PAs, incident and reflected waves are different in frequency multipliers therefore the dual input DPD model for frequency multipliers will not be same as for PAs. Moreover, in order to relax the hardware requirement for frequency-multipliers-based high frequency signal source, bandlimited DPD schemes can be investigated and devised. This will significantly reduce the DAC BW requirements. Similarly, subrate techniques with DPD can be studied in order to reduce the analog-to-digital converter (ADC) BW requirement.

At last, in order to deploy the frequency-multipliers-based single antenna or LSMA high frequency source at commercial or production level, the DPD scheme has to be implemmented in real-time. Such real time deployment which experiences a trade-off between system up-time, complexity, cost and power consumption using field programmable gate array (FPGA) or other hardware can be studied.

References

[1] A. Chung, A. M. Darwish, E. Viveiros, H. A. Hung, P. Mitran, and S. Boumaiza, "Analysis and Compensation of Nonidealities in Frequency Multiplier-Based High-Frequency Vector Signal Generators," *IEEE Transactions on Microwave Theory and Techniques*, vol. 67, no. 6, pp. 2270–2283, June 2019.

[2] T. S. Rappaport, R. W. Heath Jr, R. C. Daniels, and J. N. Murdock, *Millimeter Wave Wireless Communications*. Pearson Education, 2015.

[3] C. A. Balanis, *Antenna Theory: Analysis and Design*. John wiley & sons, 2016.

[4] M. Benisha, R. T. Prabu, and V. T. Bai, "Requirements and Challenges of 5G cellular systems," in *2016 2nd International Conference on Advances in Electrical, Electronics, Information, Communication and Bio-Informatics (AEEICB)*, Feb 2016, pp. 251–254.

[5] A. Niknejad and H. Hashemi, *mm-Wave Silicon Technology: 60 GHz and Beyond*, ser. Integrated Circuits and Systems. Springer US, 2008.

[6] K. S. Yeo and K. Ma, *Low-power Wireless Communication Circuits and Systems: 60GHz and Beyond*. Pan Stanford, 2018.

[7] K. Kibaroglu, M. Sayginer, and G. M. Rebeiz, "A Quad-Core 2832 GHz Transmit/Receive 5G Phased-Array IC with Flip-Chip Packaging in SiGe BiCMOS," in *2017 IEEE MTT-S International Microwave Symposium (IMS)*, June 2017, pp. 1892–1894.

[8] X. Gu, D. Liu, C. Baks, O. Tageman, B. Sadhu, J. Hallin, L. Rexberg, and A. Valdes-Garcia, "A Multilayer Organic Package with 64 Dual-Polarized Antennas for 28GHz 5G Communication," in *2017 IEEE MTT-S International Microwave Symposium (IMS)*, June 2017, pp. 1899–1901.

[9] H. Song, J. Kim, K. Ajito, N. Kukutsu, and M. Yaita, "50-Gb/s Direct Conversion QPSK Modulator and Demodulator MMICs for Terahertz Communications at 300 GHz," *IEEE Trans. Microw. Theory Techn.*, vol. 62, no. 3, pp. 600–609, March 2014.

[10] N. Sarmah and et al., "A Wideband Fully Integrated SiGe Chipset for High Data Rate Communication at 240 GHz," in *2016 11th European Microwave Integrated Circuits Conference (EuMIC)*, Oct 2016, pp. 181–184.

[11] K. K. Tokgoz and et al., "A 120Gb/s 16QAM CMOS Millimeter-Wave Wireless Transceiver," in *2018 IEEE International Solid - State Circuits Conference - (ISSCC)*, Feb 2018, pp. 168–170.

[12] K. K. Tokgoz and K. Okada, "Millimeter-Wave CMOS Transceiver Toward 1Tbps Wireless Communication," in *2019 IEEE International Symposium on Circuits and Systems (ISCAS)*, May 2019, pp. 1–4.

[13] C. M. Grotsch, S. Wagner, and I. Kallfass, "An Active Gate-Pumped Transconductance Upconverter for Terahertz Frequencies," in *2019 12th German Microwave Conference (GeMiC)*, March 2019, pp. 236–239.

[14] I. M. Milosavljevi, D. P. Krum, . P. Glavonji, S. P. Jovanovi, V. R. Mihajlovi, D. M. Tasovac, and V. M. Milovanovi, "A SiGe Highly Integrated FMCW Transmitter Module With a 59.5-70.5-GHz Single Sweep Cover," *IEEE Transactions on Microwave Theory and Techniques*, vol. 66, no. 9, pp. 4121–4133, Sep. 2018.

[15] P. Rodrguez-Vzquez, J. Grzyb, N. Sarmah, B. Heinemann, and U. R. Pfeiffer, "A 65 Gbps QPSK One Meter Wireless Link Operating at a 225-255 GHz Tunable Carrier in a SiGe HBT Technology," in *2018 IEEE Radio and Wireless Symposium (RWS)*, Jan 2018, pp. 146–149.

[16] P. Rodrguez-Vzquez, J. Grzyb, B. Heinemann, and U. R. Pfeiffer, "A 16-QAM 100-Gb/s 1-M Wireless Link With an EVM of 17% at 230 GHz in an SiGe Technology," *IEEE Microwave and Wireless Components Letters*, vol. 29, no. 4, pp. 297–299, April 2019.

[17] M. H. Eissa, A. Malignaggi, R. Wang, M. Elkhouly, K. Schmalz, A. C. Ulusoy, and D. Kissinger, "Wideband 240-GHz Transmitter and Receiver in BiCMOS Technology With 25-Gbit/s Data Rate," *IEEE Journal of Solid-State Circuits*, vol. 53, no. 9, pp. 2532–2542, Sep. 2018.

[18] Q. Zhong, Z. Chen, N. Sharma, S. Kshattry, W. Choi, and K. O. Kenneth, "300-GHz CMOS QPSK Transmitter for 30-Gbps Dielectric Waveguide Communication," in *2018 IEEE Custom Integrated Circuits Conference (CICC)*, April 2018, pp. 1–4.

[19] K. Katayama and et al., "20.1 A 300 GHz 40 nm CMOS Transmitter with 32-QAM 17.5Gb/s/ch Capability over 6 Channels," in *2016 IEEE International Solid-State Circuits Conference (ISSCC)*, Jan 2016, pp. 342–343.

[20] K. Takano and et al., "17.9 A 105Gb/s 300 GHz CMOS Transmitter," in *2017 IEEE International Solid-State Circuits Conference (ISSCC)*, Feb 2017, pp. 308–309.

[21] C. L. Cuccia and E. W. Matthews, "PSK and QPSK Modulators for Gigabit Data Rates," in *1977 IEEE MTT-S International Microwave Symposium Digest*, June 1977, pp. 208–211.

[22] K. B. Cooper and et al., "Submillimeter-Wave Active Radar Imager," in *2007 Joint 32nd International Conference on Infrared and Millimeter Waves and the 15th International Conference on Terahertz Electronics*, Sept 2007, pp. 922–923.

[23] J. Park, H. Ryu, K. Ha, J. Kim, and D. Baek, "76-81-GHz CMOS Transmitter With a Phase-Locked-Loop-Based Multichirp Modulator for Automotive Radar," *IEEE Trans. Microw. Theory Techn.*, vol. 63, no. 4, pp. 1399–1408, April 2015.

[24] S. Kang, S. V. Thyagarajan, and A. M. Niknejad, "A 240 GHz Fully Integrated Wideband QPSK Transmitter in 65 nm CMOS," *IEEE J. Solid-State Circuits*, vol. 50, no. 10, pp. 2256–2267, Oct 2015.

[25] J. Song, C. Cui, S. Kim, B. Kim, and S. Nam, "A Low-Phase-Noise 77-GHz FMCW Radar Transmitter With a 12.8-GHz PLL and a ×6 Frequency Multiplier," *IEEE Microw. Wireless Compon. Lett.*, vol. 26, no. 7, pp. 540–542, July 2016.

[26] A. Darwish and et. al., "Efficient Linear Transmission of Complex Waveforms at 216 GHz Using Nonlinear Multiplier Chains," in *2016 IEEE MTT-S Int. Microw. Symp. Dig.*, May 2016, pp. 1–3.

[27] A. Chung, M. B. Rejeb, A. Darwish, H. Hung, and S. Boumaiza, "Frequency Doubler Based Outphasing System for Millimeter Wave Vector Signal Generation," in *2018 48th European Microwave Conference (EuMC)*, Sep. 2018.

[28] D. Cox and R. Leck, "Component Signal Separation and Recombination for Linear Amplification with Nonlinear Components," *IEEE Transactions on Communications*, vol. 23, no. 11, pp. 1281–1287, November 1975.

[29] Y. Park and J. S. Kenney, "Adaptive digital predistortion linearization of frequency multipliers."

[30] Y. Park, R. Melville, R. C. Frye, M. Chen, and J. S. Kenney, "Dual-Band Transmitters Using Digitally Predistorted Frequency Multipliers for Reconfigurable Radios," *IEEE Trans. Microw. Theory Techn.*, vol. 53, no. 1, pp. 115–122, Jan. 2005.

[31] J. H. Choi, S. M. Kang, and K. H. Koo, "Digital Predistortion of Frequency Multiplier for Dual Band Wireless LAN Transmitter," in *IEEE MTT-S Int. Microwave Symp. Dig.*, Jun. 2005, p. 4.

[32] S. M. Kang, S. W. Nam, and K. H. Koo, "Adaptive Linearization of Frequency Doubler Using DGS," in *2007 IEEE/MTT-S International Microwave Symposium*, June 2007, pp. 1225–1228.

[33] Y. Zhao and et al., "Digital Predistortion of 75-110 GHz W-Band Frequency Multiplier for Fiber Wireless Short Range Access Systems," *Opt. Express*, vol. 19, no. 26, pp. B18–B25, Dec 2011.

[34] Y. R. Ramadan, M. Abdelgelil, and H. Minn, "Novel Pre-Compensation Schemes for Low-Cost Nonlinear Tera-Hertz Transmitters," in *2018 IEEE International Conference on Communications (ICC)*, May 2018, pp. 1–6.

[35] Y. R. Ramadan, H. Minn, and M. E. Abdelgelil, "Precompensation and System Parameters Estimation for Low-Cost Nonlinear Tera-Hertz Transmitters in the Presence of I/Q Imbalance," *IEEE Access*, vol. 6, pp. 51 814–51 833, 2018.

[36] Y. Liu, G. Liu, and P. M. Asbeck, "High-Order Modulation Transmission Through Frequency Quadrupler Using Digital Predistortion," *IEEE Trans. Microw. Theory Techn.*, vol. 64, no. 6, pp. 1896–1910, Jun. 2016.

[37] D. Nopchinda, Z. He, G. Granstrom, M. Gavell, and H. Zirath, "8-PSK Upconverting Transmitter Using E-Band Frequency Sextupler," *IEEE Microw. Wireless Compon. Lett.*, vol. 28, no. 2, pp. 177–179, Feb 2018.

[38] A. Chung, M. B. Rejeb, Y. Beltagy, A. Darwish, H. Hung, and S. Boumaiza, "High Frequency and Wideband Modulated Signal Generation Using Frequency Doublers," in *2018 IEEE MTT-S Int. Microw. Symp. Dig.*, Jun. 2018.

[39] B. Fehri and S. Boumaiza, "Systematic Estimation of Memory Effects Parameters in Power Amplifiers' Behavioral Models," in *2011 IEEE MTT-S International Microwave Symposium*, June 2011, pp. 1–4.

[40] R. N. Braithwaite, "Memory Correction of a Doherty Power Amplifier with a WCDMA Input Using Digital Predistortion," in *2006 IEEE MTT-S International Microwave Symposium Digest*, June 2006, pp. 1526–1529.

[41] L. Ding, F. Mujica, and Z. Yang, "Digital Predistortion Using Direct Learning with Reduced Bandwidth Feedback," in *2013 IEEE MTT-S International Microwave Symposium Digest (MTT)*, June 2013, pp. 1–3.

[42] U. R. Pfeiffer and D. Goren, "A 23-dBm 60-GHz Distributed Active Transformer in a Silicon Process Technology," *IEEE Transactions on Microwave Theory and Techniques*, vol. 55, no. 5, pp. 857–865, May 2007.

72

[43] Y. Jen, J. Tsai, T. Huang, and H. Wang, "Design and Analysis of a 5571-GHz Compact and Broadband Distributed Active Transformer Power Amplifier in 90-nm CMOS Process," *IEEE Transactions on Microwave Theory and Techniques*, vol. 57, no. 7, pp. 1637–1646, July 2009.

[44] C. Y. Law and A. Pham, "A High-Gain 60GHz Power Amplifier with 20dBm Output Power in 90nm CMOS," in *2010 IEEE International Solid-State Circuits Conference - (ISSCC)*, Feb 2010, pp. 426–427.

[45] Y. Jiang, J. Tsai, and H. Wang, "A W-Band Medium Power Amplifier in 90 nm CMOS," *IEEE Microwave and Wireless Components Letters*, vol. 18, no. 12, pp. 818–820, Dec 2008.

[46] Y. A. Atesal, B. Cetinoneri, M. Chang, R. Alhalabi, and G. M. Rebeiz, "Millimeter-Wave Wafer-Scale Silicon BiCMOS Power Amplifiers Using Free-Space Power Combining," *IEEE Transactions on Microwave Theory and Techniques*, vol. 59, no. 4, pp. 954–965, April 2011.

[47] F. Golcuk, T. Kanar, and G. M. Rebeiz, "A 90100 Ghz 44 SiGe BiCMOS Polarimetric Transmit-Receive Phased Array with Simultaneous Receive-Beams Capabilities," in *2013 IEEE International Symposium on Phased Array Systems and Technology*, Oct 2013, pp. 102–105.

[48] J. Harvey, E. R. Brown, D. B. Rutledge, and R. A. York, "Spatial Power Combining for High-Power Transmitters," *IEEE Microwave Magazine*, vol. 1, no. 4, pp. 48–59, Dec 2000.

[49] R. A. York and Z. B. Popović, *Active and Quasi-Optical Arrays for Solid-State Power Combining*. Wiley New York, 1997.

[50] M. A. Gouker, J. T. Delisle, and S. M. Duffy, "A Circuit-Fed Tile-Approach Configuration for Millimeter-Wave Spatial Power Combining," *IEEE Transactions on Microwave Theory and Techniques*, vol. 50, no. 1, pp. 17–21, Jan 2002.

[51] M. P. DeLisio, B. C. Deckman, Chun-Tung Cheung, S. C. Martin, C. J. Rollison, J. J. Rosenberg, G. Smith, and J. Eisenberg, "Power and Spectral Regrowth Performance of 10-W and 16-W Ka-Band Power Amplifiers with Single-Chip Output Stages," in *IEEE MTT-S International Microwave Symposium Digest, 2005.*, June 2005, pp. 4 pp.–842.

[52] Younkyu Chung, Chun-Tung Cheung, M. P. DeLisio, and D. B. Rutledge, "W-Band Waveguide-Packaged InP HEMT Reflection Grid Amplifier," *IEEE Microwave and Wireless Components Letters*, vol. 16, no. 6, pp. 324–326, June 2006.

[53] M. A. Gouker, "A Circuit-Fed, Tile-Approach Configuration for Millimeter-Wave Spatial Power Combining," in *1999 SBMO/IEEE MTT-S International Microwave and Optoelectronics Conference*, vol. 1, Aug 1999, pp. 231–232 vol. 1.

[54] J. B. Hacker, A. L. Sailer, B. Brar, G. Nagy, R. L. J. Pierson, and J. A. Higgins, "A High-Power W-Band Quasi-Optical Frequency Tripler," in *IEEE MTT-S International Microwave Symposium Digest, 2003*, vol. 3, June 2003, pp. 1859–1862 vol.3.

[55] E. Öjefors, J. Grzyb, Y. Zhao, B. Heinemann, B. Tillack, and U. R. Pfeiffer, "A 820GHz SiGe Chipset for Terahertz Active Imaging Applications," in *2011 IEEE International Solid-State Circuits Conference.* IEEE, 2011, pp. 224–226.

[56] X. Deng, Y. Li, J. Li, C. Liu, W. Wu, and Y. Xiong, "A 320-GHz 1×4 Fully Integrated Phased Array Transmitter Using 0.13-μm SiGe BiCMOS Technology," *IEEE Transactions on Terahertz Science and Technology*, vol. 5, no. 6, pp. 930–940, Nov 2015.

[57] Y. Yang, O. D. Gurbuz, and G. M. Rebeiz, "An Eight-Element 370-410-GHz Phased-Array Transmitter in 45-nm CMOS SOI With Peak EIRP of 88.5 dBm," *IEEE Transactions on Microwave Theory and Techniques*, vol. 64, no. 12, pp. 4241–4249, Dec 2016.

[58] R. Klimovich, S. Jameson, and E. Socher, "Coherent J-Band Radiating Arrays Based on ×27 CMOS Activemultiplier Chips," *International Journal of Microwave and Wireless Technologies*, pp. 1–8, 2019.

[59] S. Lee, M. Kim, Y. Sirl, E. Jeong, S. Hong, S. Kim, and Y. H. Lee, "Digital Predistortion for Power Amplifiers in Hybrid MIMO Systems with Antenna Subarrays," in *2015 IEEE 81st Vehicular Technology Conference (VTC Spring)*, May 2015, pp. 1–5.

[60] L. Liu, W. Chen, L. Ma, and H. Sun, "Single-PA-Feedback Digital Predistortion for Beamforming MIMO Transmitter," in *2016 IEEE International Conference on Microwave and Millimeter Wave Technology (ICMMT)*, vol. 2, June 2016, pp. 573–575.

[61] N. Tervo, J. Aikio, T. Tuovinen, T. Rahkonen, and A. Parssinen, "Digital Predistortion of Amplitude Varying Phased Array Utilising Over-The-Air Combining," in *2017 IEEE MTT-S International Microwave Symposium (IMS)*, June 2017, pp. 1165–1168.

[62] E. Ng, Y. Beltagy, P. Mitran, and S. Boumaiza, "Single-Input Single-Output Digital Predistortion of Power Amplifier Arrays in Millimeter Wave RF Beamforming Transmitters," in *2018 IEEE/MTT-S International Microwave Symposium - IMS*, June 2018, pp. 481–484.

[63] K. Hausmair, P. N. Landin, U. Gustavsson, C. Fager, and T. Eriksson, "Digital Predistortion for Multi-Antenna Transmitters Affected by Antenna Crosstalk," *IEEE Transactions on Microwave Theory and Techniques*, vol. 66, no. 3, pp. 1524–1535, March 2018.

[64] E. Ng, Y. Beltagy, G. Scarlato, A. Ben Ayed, P. Mitran, and S. Boumaiza, "Digital Predistortion of Millimeter-Wave RF Beamforming Arrays Using Low Number of Steering Angle-Dependent Coefficient Sets," *IEEE Transactions on Microwave Theory and Techniques*, vol. 67, no. 11, pp. 4479–4492, Nov 2019.